An update to this article is included at the end

Journal of Molecular Liquids 299 (2020) 112165

Contents lists available at ScienceDirect

Journal of Molecular Liquids

journal homepage: www.elsevier.com/locate/molliq

A new approach for coupled modelling of the structural and thermo-physical properties of molten salts. Case of a polymeric liquid LiF-BeF_2

A.L. Smith[a,*], E. Capelli[a], R.J.M. Konings[b], A.E. Gheribi[c]

[a] Delft University of Technology, Faculty of Applied Sciences, Radiation Science & Technology Department, Mekelweg 15, Delft 2629 JB, the Netherlands
[b] European Commission, Joint Research Centre (JRC), Directorate for Nuclear Safety and Security, Postfach 2340, Karlsruhe D-76125, Germany
[c] Centre for Research in Computational Thermochemistry, Department of Chemical Engineering, Ecole Polytechnique, C.P. 6079, Succursale "Downtown", Montreal, Quebec H3C 3A7, Canada

ARTICLE INFO

Article history:
Received 18 July 2019
Received in revised form 12 October 2019
Accepted 17 November 2019
Available online 21 November 2019

Keywords:
Molecular dynamics (Polarizable Ion Model)
CALPHAD
Fluoride salts
Polymeric liquid

ABSTRACT

The (Li,Be)F_x fluoride salt is an ionic liquid with complex non-ideal thermodynamic behaviour due to the formation of short-range order. In this work, we explore the relationship between local structure, thermo-physical and thermodynamic properties in this system using a multidisciplinary approach that couples molecular dynamics simulations using the Polarizable Ion Model (PIM) and thermodynamic modelling assessment using the CALPHAD method. The density, thermal expansion, viscosity, thermal conductivity, molar and mixing enthalpies and heat capacity of the (Li,Be)F_x melt are extracted from the polarizable ionic interaction potentials and investigated across a wide range of compositions and temperatures. The agreement with the available experimental data is generally very good. The local structure is also examined in detail, in particular the transition between a molecular liquid with Li^+, BeF_4^{2-} and F^- predominant species at low BeF_2 content, and a polymeric liquid at high BeF_2 content, with the formation of polymers ($Be_2F_7^{3-}$, $Be_3F_{10}^{4-}$, $Be_4F_{13}^{5-}$, etc.), and finally of a three-dimensional network of corner-sharing tetrahedrally coordinated Be^{2+} cations for pure BeF_2. Based on the available experimental information and the output of the MD simulations, we moreover develop for the first time a coupled structural-thermodynamic model for the LiF-BeF_2 system based on the quasi-chemical formalism in the quadruplet approximation, that provides a physical description of the melt and reproduces (in addition to the thermodynamic data) the chemical speciation of beryllium polymeric species predicted from the simulations.

© 2019 The Authors. Published by Elsevier B.V. This is an open access article under the CC BY license (http://creativecommons.org/licenses/by/4.0/).

1. Introduction

The LiF-BeF_2 system has been widely investigated in the past due to its importance for the development of the Molten Salt Reactor technology and because of its interesting and peculiar structural properties from theoretical perspectives. ^{7}LiF-BeF_2 (FLIBE) was selected as fuel carrier for the Molten Salt Reactor Experiment (MSRE) in 1965–1969 [1] due to its favorable neutronic and thermo-physical properties, and is nowadays still a primary choice for some Molten Salt Reactor (MSR) designs or as primary coolant in Advanced High Temperature Reactors (AHTRs) [1,2]. In addition, it is also one of the options for liquid blanket systems in fusion reactors [3].

Studies on beryllium fluoride systems in general have also been numerous as BeF_2(cr) adopts a structure analogue to SiO_2(cr), with a three-dimensional network of corner-sharing tetrahedrally coordinated Be^{2+} cations, but with a much lower melting temperature which makes experiments with BeF_2 on some aspects less demanding. The liquid moreover shows a polymeric structure similar to silicate melts, and its connectivity is reduced by adding alkali fluorides such as LiF, in a similar way to the behaviour observed when adding alkali or alkaline-earth oxides to SiO_2.

Fluoride salts are ionic liquids in which cations and anions form a loose network [1]. Depending on conditions of composition, temperature and concentration, they can form a dissociated ionic melt, molecular species or exhibit polymerization [4,5]. The formation of short-range order in the liquid contributes to storing energy in the salt and to thermodynamic excess properties. In this work, we explore this relationship and report a comprehensive model coupling structure, thermodynamic, and thermo-physical properties in the LiF-BeF_2 system, illustrating the case of a polymeric liquid.

The experimental studies performed on the LiF-BeF_2 system include thermodynamic investigations of phase diagram equilibria, mixing enthalpies, activity coefficients, heat capacities, vapour

* Corresponding author.
E-mail address: a.l.smith@tudelft.nl (A. Smith).

https://doi.org/10.1016/j.molliq.2019.112165
0167-7322/© 2019 The Authors. Published by Elsevier B.V. This is an open access article under the CC BY license (http://creativecommons.org/licenses/by/4.0/).

pressures [6-14], density and viscosity [15,16], thermal diffusivity and thermal conductivity of the melt at high temperatures [13,17,18]. Thermodynamic modelling assessments using the CALPHAD method (CALculation of PHAse Diagram) [19] have been reported by Van der Meer [20] using Redlich-Kister polynomials, and later by Beneš and Konings using the quasi-chemical model in the quadruplet approximation [21]. Around the same time, Romero-Serrano et al. [22] reported a "structural" thermodynamic model for this system similar to that previously applied to silicate melts AO-SiO_2 (A = Ca, Mn, Mg, Fe, etc.) [23,24], based on empirical expressions for enthalpy and non-configurational excess entropy. Finally, molecular dynamics studies by Heaton et al. [25] and Salanne et al. [26,27] using the Polarizable Ion Model (PIM) should be mentioned, where the interaction potentials of BeF_2 and its mixture with LiF were obtained from first-principles calculations on the condensed phases. The authors compared the predicted thermo-physical properties of pure BeF_2 (diffraction, infrared, diffusion data) and of the molten salt mixtures at selected temperatures and compositions (vibrational spectra, electrical conductivity, viscosity) with the available experimental data, with good results, thereby demonstrating the promising predictive capabilities of their method.

Hereafter, we calculate the thermo-physical properties of the LiF-BeF_2 system based on the reported interaction potentials of the Polarizable Ion Model (PIM), covering a wider range of compositions and temperatures than done previously in Refs.[26,27]: (i) density, (ii) thermal expansion, (iii) viscosity, and (iv) thermal conductivity are calculated and compared to the available experimental data. We also derive the thermodynamic properties of the molten salt for the first time from the MD potentials: (v) molar enthalpy and enthalpy of mixing, (vi) heat capacity and excess heat capacity. In addition, we characterize in detail the (local) structure of the melt at selected temperatures. Because molecular dynamics are not well suited to characterize phase equilibria, the aim of this work is to subsequently combine the output of the MD simulations with a CALPHAD assessment of the system, so as to provide in the end a comprehensive picture of the structure-property relationships in the (Li,Be)F_x polymeric melt.

2. Molecular dynamics simulations: the Polarizable Ion Model

The Polarizable Ion Model (PIM) used in the present work and developed by Madden and co-workers, is a particularly well-suited simulation method for fluoride and chloride salts [4, 28-30]. This method is based on a semi-classical approach where the interaction potentials between given pairs of ions are derived ab initio from electronic structure calculations on the condensed phases [28]. Only the density of the pure compounds are necessary as first input [4]. The interaction potentials include both classical interaction forces, i.e. charge-charge V_{qq}, repulsion V_{rep}, dispersion V_{disp} and those resulting from polarization effects V_{pol} [4]. Their functional form are given by the following equations:

$$V_{qq}(r_{ij}) = \Sigma_{i<j} \frac{q_i q_j}{r_{ij}} \tag{1}$$

where q_i and q_j are the formal charges of ions i and j.

$$V_{rep}(r_{ij}) = \Sigma_{i<j} A^{ij} e^{-a_{ij} r_{ij}} \tag{2}$$

where A_{ij} and a_{ij} are fitting parameters.

$$V_{disp}(r_{ij}) = -\Sigma_{i<j} \left[f_{ij}^6(r_{ij}) \frac{C_{ij}^6}{r_{ij}^6} + f_{ij}^8(r_{ij}) \frac{C_{ij}^8}{r_{ij}^8} \right] \tag{3}$$

where C_{ij}^6 and C_{ij}^8 are the dipole-dipole and dipole-quadrupole dispersion coefficients, respectively. f_{ij}^6 and f_{ij}^8 correspond to Tang-Toennies dispersion damping functions that account for short-range correction to the asymptotic multipole expansion of dispersions. They are given by the equation:

$$f_{ij}^n(r_{ij}) = 1 - e^{-\left(b_{ij}^n r_{ij}\right)} \Sigma_{k=0}^n \frac{\left(b_{ij}^n r_{ij}\right)^k}{k!} \tag{4}$$

in which b_{ij} equals the distance at which the correction factor is applied.

$$V_{pol}(r_{ij}) = \Sigma_{i<j} \left[q_i \mu_{j\alpha} g_{ij}(r_{ij}) - q_i \mu_{i\alpha} g_{ij}(r_{ij}) \right] T_\alpha^{(1)}(r_{ij}) - \Sigma_{i<j} \mu_{i\alpha} \mu_{j\beta} T_{\alpha\beta}^{(2)}(r_{ij}) + \Sigma_i \frac{1}{2\alpha_i} |\mu_i|^2 \tag{5}$$

where $T_\alpha^{(1)}$ is the charge-dipole interaction tensor, $T_{\alpha\beta}^{(2)}$ is the dipole-dipole interaction tensor, α_i the polarizability of ion i, and μ_i the set of induced dipoles, thereby introducing $3N$ additional degrees of freedom to the system.

The interaction potential parameters for the (Li,Be)F_x liquid solution, treated as a mixture of Li^+, Be^{2+} and F^- ions, have been determined by Heaton et al. [25]. They are listed in Table 1. Note that the A_{ij} and a_{ij} parameters were not reported correctly in the paper by Ref. [25]. The polarization term accounts for fluoride polarization only, with a fluoride polarizability equal to 7.09 $Bohr^3$. The parameters of the damping function are: $b_{FBe} = 1.78$, $b_{FLi} = 1.81$, $c_{FBe} = 0.99$ and $c_{FLi} = 1.40$.

Two simulation cells were used to rule out any size effects: one with a total of 550 ions, and the other with a total of 800 ions. The assessed temperatures and compositions are listed in Table 2. The systems were equilibrated for 1 ns in the NPT ensemble at 0 GPa, from which the equilibrium volumes were taken. This was followed by 200 ps of equilibration in the NVT ensemble, and finally 5 to 10–20 ns production run for each temperature and composition. Longer runs were used for compositions above $x(BeF_2) = 0.6$ and lower temperatures to make sure the shear stress autocorrelation function and microscopic fluxes autocorrelation function reached a plateau for the calculation of the viscosity and thermal conductivity via a Green-Kubo formalism (see Sections 4.1.5 and 4.1.6). Time steps in both ensemble were set to 0.5 fs, whereas the relaxation time for both the Nosé-Hoover thermostat and barostat (for the NPT run) was set to 10 ps. Cutoffs for the real space part of the Ewald sum and short-range potential were both set to half the length of the cell.

3. Thermodynamic modelling: the quasi-chemical formalism in the quadruplet approximation

The thermodynamic modelling assessment of the LiF-BeF_2 system is carried out using the CALPHAD (CALculation of Phase Diagram) method, based on the least-square minimization of the total Gibbs energy of the system [19] using the Factsage software [31]. Both the experimental data reported in the literature and the output of the

Table 1
Parameter values for the LiF-BeF_2 potentials, given in atomic units. The atomic unit of length is the Bohr radius (0.52918 Å), the atomic unit of energy the Hartree ($4.3597 \cdot 10^{-18}$ J).

Ion pair	A_{ij}	a_{ij}	C_{ij}^6	C_{ij}^8	b_{ij}^6	b_{ij}^8
F^--F^-	181.84	2.267	15.0	150.0	1.9	1.9
Be^{2+}-F^-	41.72	2.254	0.0	0.0	1.0	1.0
Li^+-F^-	20.42	2.052	0.0	0.0	1.0	1.0
Be^{2+}-Be^{2+}	106.16	3.944	0.0	0.0	1.0	1.0
Be^{2+}-Li^+	0.0	1.0	0.0	0.0	1.0	1.0
Li^+-Li^+	195.91	4.252	0.0	0.0	1.0	1.0

Table 2
Molecular dynamics simulations conditions.

$x(BeF_2)$	N_{F^-}	$N_{Be^{2+}}$	N_{Li^+}	N_{total}	T (K)
0	275	0	275	550	600/700/800/900/1000/1100/1135/1200
0.049	281	13	255	549	900/1135/1200
0.099	288	26	236	550	900/1135/1200
0.148	294	38	218	550	900/1135/1200
0.2	300	50	200	550	600/700/800/900/1000/1100/1135/1200
0.25	305	61	183	549	900/1135/1200
0.301	311	72	167	550	900/1135/1200
0.33	314	78	158	550	753/778/828/878/1135/1200
0.35	316	82	152	550	900/1135/1200
0.397	320	91	138	549	600/700/800/900/1000/1100/1135/1200
0.451	325	101	123	549	900/1135/1200
0.5	330	110	110	550	670/695/745/795/900/945/975/1135/1200
0.507	330	111	108	549	600/700/800/900/1000/1100/1135/1200
0.553	334	119	96	549	900/1135/1200
0.602	338	127	84	549	600/700/800/900/1000/1100/1135/1200
0.652	342	135	72	549	900/1135/1200
0.704	346	143	60	549	900/1135/1200
0.75	350	150	50	550	818/843/893/900/943/1135/1200
0.801	353	157	39	549	600/700/800/900/1000/1100/1135/1200
0.85	357	164	29	550	900/1135/1200
0.905	360	171	18	549	900/1135/1200
0.952	363	177	9	549	900/1135/1200
1	366	183	0	549	600/700/800/900/1000/1100/1135/1200
0	400	0	400	800	800/900/1000/1100/1200
0.094	418	36	346	800	800/900/1000/1100/1200
0.203	437	74	289	800	700/800/900/1000/1100/1200
0.332	457	114	229	800	600/700/800/900/1000/1100/1200
0.439	472	144	184	800	600/700/800/900/1000/1100/1200
0.532	484	168	148	800	600/700/800/900/1000/1100/1200
0.64	497	194	109	800	600/700/800/900/1000/1100/1200
0.749	509	218	73	800	600/700/800/900/1000/1100/1200
0.857	520	240	40	800	600/700/800/900/1000/1100/1200
0.996	533	266	1	800	600/700/800/900/1000/1100/1200

MD simulations were used to adjust the excess parameters of the Gibbs energy functions of the phases involved in this system.

3.1. Stoichiometric compounds

The Gibbs energy function of a pure condensed phase is defined as:

$$G(T) = \Delta_f H^o_m(298) - S^o_m(298)T + \int_{298}^{T} C_{p,m}(T)dT - T\int_{298}^{T} \frac{C_{p,m}}{T}dT \quad (6)$$

where $\Delta_f H^o_m(298)$ is the standard enthalpy of formation, $S^o_m(298)$ is the standard absolute entropy, both evaluated at a standard temperature of 298.15 K (noted 298 K throughout this work for simplicity), and $C_{p,m}$ is the isobaric heat capacity expressed as a polynomial:

$$C_{p,m}(T) = a + bT + cT^2 + dT^{-2} + eT^3 \quad (7)$$

The LiF-BeF_2 system involves four solid phases, namely the two end-members LiF and BeF_2, and two intermediate compounds Li_2BeF_4 and $LiBeF_3$. Their thermodynamic data are listed in Table 3. The well-known data for the end-members were taken from the literature. BeF_2 shows two polymorphs of quartz, i.e. a low temperature α and a high temperature β forms with a phase transition at $T_{tr} = 500$ K and associated transition enthalpy equal to $\Delta_{tr}H^o_m = 284\,J\cdot mol^{-1}$ in the present model based on the critical review by Konings et al. [32]. The selected melting temperature and melting enthalpy for BeF_2 in the latter review [32], i.e. $T_{fus} = (828 \pm 5)$ K and $\Delta_{fus}H^o_m = (4.5 \pm 0.2)\,kJ\cdot mol^{-1}$, are also retained for our model. Note that those values differ slightly from the recommended data by NIST-JANAF [33] ($T_{tr} = 500$ K, $\Delta_{tr}H^o_m = 220\,J\cdot mol^{-1}$, $T_{fus} = 825$ K, $\Delta_{fus}H^o_m = 4.757\,kJ\cdot mol^{-1}$). The standard enthalpy of formation, standard entropy, and heat capacity functions for the intermediate compounds Li_2BeF_4(cr) and $LiBeF_3$(cr) were taken from the NIST-JANAF tables [33], and the entropy terms slightly adjusted compared to the original values (130.583 and 89.245 $J\cdot K^{-1}\cdot mol^{-1}$, respectively) to reproduce the expected melting temperatures in the phase diagram.

3.2. Liquid solution

The excess Gibbs energy terms of the liquid solution are modelled in this work using the modified quasi-chemical model proposed by Pelton et al. [35] in the quadruplet approximation. In the latter approximation, a quadruplet composed of two cations A and B and two anions (fluorine F in this case is the only anion present), is assumed to be the basic unit in the liquid solution (Fig. 1).

The optimized excess parameters of the liquid solution are linked to the second-nearest neighbour (SNN) exchange reaction of the quadruplets and is expressed as:

$$(A-F-A) + (B-F-B) \longrightarrow 2(A-F-B) \quad (8)$$

The Gibbs energy change $\Delta g_{AB/F}$ associated with this SNN exchange reaction is given by:

$$\Delta g_{AB/F} = \Delta g^o_{AB/F} + \sum_{i\geq 1} g^{i0}_{AB/F}\chi^i_{AB/F} + \sum_{j\geq 1} g^{0j}_{AB/F}\chi^j_{BA/F} \quad (9)$$

where $\Delta g^o_{AB/F}$ and $g^{ij}_{AB/F}$ are composition independent coefficients that may vary with temperature.

The composition dependence $\chi^i_{AB/F}$ is a function of the cation-cation pair mole fractions X_{AA}, X_{BB}, and X_{AB}:

$$\chi_{AB/F} = \frac{X_{AA/F_2}}{X_{AA/F_2} + X_{AB/F_2} + X_{BB/F_2}} \quad (10)$$

Table 3
Thermodynamic data for end-members and intermediate compounds used in this work for the phase diagram assessment: $\Delta_f H^o_m(298\,K)/(kJ \cdot mol^{-1})$, $S^o_m(298\,K)/(J \cdot K^{-1} \cdot mol^{-1})$, and heat capacity coefficients $C_{p,m}(T/K)/(J \cdot K^{-1} \cdot mol^{-1})$, where $C_{p,m}(T/K) = a + b \cdot T + c \cdot T^2 + d \cdot T^{-2} + e \cdot T^3$. Optimized data are shown in **bold**.

Compound	$\Delta_f H^o_m(298\,K)/(kJ \cdot mol^{-1})$	$S^o_m(298\,K)/(J \cdot K^{-1} \cdot mol^{-1})$	$C_{p,m}(T/K)/(J \cdot K^{-1} \cdot mol^{-1}) = a + b \cdot T + c \cdot T^2 + d \cdot T^{-2} + e \cdot T^3$					T/K	Ref.
			a	b	c	d	e		
LiF(cr)	−616.931	35.66	43.309	0.016312	$5.0470 \cdot 10^{-7}$	−569,123.6		298.15–1500	[33]
LiF(l)	−598.654	42.962	64.183					298.15–2500	[33]
LiF(g)	−340.946	200.188	35.397917	0.001870664	$-1.654306 \cdot 10^{-7}$			298.15–6000	[33]
BeF_2(cr, α)	−1026.800	53.35	19.181	0.109538				298.15–500	[32]
BeF_2(cr, β)	−1025.511	56.21	39.4569	0.046255				298.15–1500	[32]
BeF_2(l)[a]	−971.427	60.79	40.9844	0.044936				298.15–2500	[32], This work
BeF_2(g)	−796.010	227.56	29.74683	0.07466	$-6.99886 \cdot 10^{-5}$		$2.43404 \cdot 10^{-8}$	298.15–1050	[33]
			61.44717	0.00033		−3,056,474.6686		1050–2000	[33]
Be_2F_4(l)[a]	−1992.854	121.6	81.9688	0.089872				298.15–2500	This work
Be_2F_4(g)	−1731.716	323.161	83.4006	0.0860764	$-4.39494 \cdot 10^{-5}$	−912,416		298.15–700	[34]
			130.4974	0.00135	$-1.896 \cdot 10^{-7}$	−5,437,627		700–3900	[34]
Be_3F_6(l)[a]	−3064.281	182.4	122.9532	0.134808				298.15–2500	This work
Li_2BeF_4(cr)	−2273.589	**132.0**	90.779451	0.1491498	$-1.8415736 \cdot 10^{-8}$	197,083.29		298.15–1500	[33], This work
$LiBeF_3$(cr)	−1651.843	**90.13**	54.39217	0.12552				298.15–1500	[33], This work
$LiBeF_3$(g)	−1390.300	292.583	−3.71166	0.30325	−0.000324686		$1.25972 \cdot 10^{-7}$	298.15–840	[33]
			106.40356	0.00063		−7,305,978.79		840–2000	[33]
Li_2F_2(g)	−935.323	261.802	83.09363	$1 \cdot 10^{-5}$		−2,170,730		298.15–6000	[33]
Li_3F_3(g)	−1524.598	316.702	132.92431	$3 \cdot 10^{-5}$		−3,747,000.5		298.15–6000	[33]

[a] Liquid beryllium fluoride is modelled as a {Be_3F_6(l)-Be_2F_4(l)-BeF_2(l)} mixture with $g^o_{Be_{IV}F_2(l)} = {}^1/_3 g^o_{Be_3F_6(l)} + 50{,}000$ and $g^o_{Be_2F_4(l)} = {}^2/_3 g^o_{Be_3F_6(l)} + 50{,}000$.

One strength of this type of formalism is the ability to select the composition of maximum short-range ordering, where the total Gibbs energy of the system has its minimum, usually around the lowest melting point of the liquidus curve. This is done by varying the ratio between cation-cation coordination numbers Z^A_{AB/F_2} and Z^B_{AB/F_2} to match in first approximation the eutectic composition. The anion-anion coordination number is subsequently fixed to satisfy conservation of charge:

$$\frac{q_A}{Z^A_{AB/F_2}} + \frac{q_B}{Z^B_{AB/F_2}} = \frac{q_F}{Z^F_{AB/F_2}} + \frac{q_F}{Z^F_{AB/F_2}} \tag{11}$$

The thermodynamic model as detailed above does not provide a truly physical description of the local structure of the salt melt, however, as we know from Raman studies [36,37], molecular dynamic simulations [25-27] and Density Functional Theory (DFT) calculations [38,39] that the (Li,Be)F_x melt tends to form molecular species and even exhibits polymerization towards higher BeF_2 concentrations. The Raman spectra of Quist et al. on molten Li_2BeF_4, Na_2BeF_4 and (LiF:NaF:BeF_2) = (0.3:0.53:0.17) melt showed the presence of tetrahedral BeF_4^{2-} complexes [36], while Toth et al. also reported the occurrence of $Be_2F_7^{3-}$ dimers in addition to BeF_4^{2-} in LiF-BeF_2 and LiF-NaF-BeF_2 molten salt mixtures [37]. These results were confirmed in the MD simulations of Heaton, Salanne and co-workers using the PIM model [25-27], indicating the formation of BeF_4^{2-}, $Be_2F_7^{3-}$, $Be_3F_{10}^{4-}$, $Be_4F_{13}^{5-}$, and higher degree polymers at high BeF_2 content. The ab initio molecular dynamics simulations of Dai et al. [39] of the local structure and IR (infrared) vibrational spectra of Li_2BeF_4 in the gas phase, in the melt at 873 K and 30 K (frozen melt) also identified BeF_4^{2-}, $Be_2F_7^{3-}$, and $Be_3F_{10}^{4-}$ entities. The same composition was investigated by Liu et al. by combining high temperature (in-situ) IR absorption spectroscopy measurements at 873 K and DFT calculations to simulate the IR spectrum [38]. The authors confirmed once again the formation of BeF_4^{2-} complexes, and ruled out the existence of BeF_3^- entities. Melts rich in LiF are thus constituted of Li^+, F^- and BeF_4^{2-} ions, while the fraction of polymeric units increases with the BeF_2 concentration until a fully connected network of corner-sharing beryllium cations is obtained for pure BeF_2, in a similar manner to the situation observed in silicate melts.

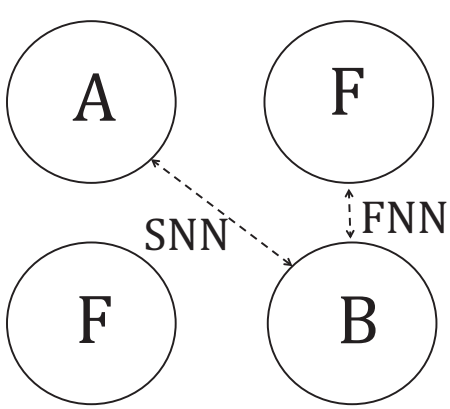

Fig. 1. Schematic representation of the quadruplet basic unit and first-nearest neighbour (FNN) and second-nearest neighbour (SNN) interactions between ions of opposite and same charge, respectively.

In this work, a coupled structural-thermodynamic description of the melt is thus proposed where the liquid solution corresponds to a mixture of fluorine anions F^-, lithium cations Li^+, and Be^{2+}_{IV}, Be^{4+}_2, and Be^{6+}_3 cations with coordinations [IV], [VII] and [X], respectively. Be^{4+}_2 and Be^{6+}_3 cations correspond to the dimer and trimer species $Be_2F_7^{3-}$, $Be_3F_{10}^{4-}$, respectively. Three compositions of maximum short-range ordering are subsequently defined. A similar physical model was reported for the ($NaF + AlF_3 + CaF_2 + BeF_2 + Al_2O_3 + BeO$) system by Robelin and Chartrand [34], which included (Na^+, Al^{3+}_V, Al^{3+}_{IV}, Al^{6+}_2, Ca^{2+}, Be^{2+}_{IV}, Be^{4+}_2) cations and (F^-, O^{2-}) anions, although this was not coupled to MD simulations.

The chemical speciation in the (Li,Be)F_x melt was first calculated in this work using the PIM model parameters listed in Section 2, by applying the methodology described in detail in Section 4.1.3 at temperatures T = 900, 1000, 1100, 1135 and 1200 K. The distribution of species calculated by MD showed Li^+, BeF_4^{2-} and F^- species at low BeF_2 content, and the formation of polymeric species $Be_2F_7^{3-}$, $Be_3F_{10}^{4-}$, $Be_4F_{13}^{5-}$, etc. with increasing BeF_2 concentration, until a fully connected network of tetrahedral corner-sharing Be^{2+} cations linked by F^- anions was obtained for pure BeF_2 (see Section 4.1.3). To reproduce the structure of the melt, while keeping a reasonable number

of fitting excess parameters, $Be_3F_{10}^{4-}$ was assumed to represent the largest possible polymeric unit in the present CALPHAD model. Hence pure beryllium fluoride is modelled with a fully connected network constituted exclusively of trimers.

To this end, the following constraints are applied to the Gibbs energy associated with the reactions $^1/_3\ Be_3F_6(l) \rightleftharpoons Be_{IV}F_2(l)$ and $^2/_3\ Be_3F_6(l) \rightleftharpoons Be_2F_4(l)$:

$$g^o_{Be_{IV}F_2(l)} = {}^1/_3 g^o_{Be_3F_6(l)} + 50{,}000\ \mathrm{J{\cdot}mol^{-1}} \tag{12}$$

$$g^o_{Be_2F_4(l)} = {}^2/_3 g^o_{Be_3F_6(l)} + 50{,}000\ \mathrm{J{\cdot}mol^{-1}} \tag{13}$$

where $g^o_{Be_{IV}F_2(l)}$, $g^o_{Be_2F_4(l)}$ and $g^o_{Be_3F_6(l)}$ are the Gibbs energies of (hypothetical) liquids made of solely Be_{IV}^{2+}, Be_2^{4+}, or Be_3^{6+} cations, respectively. The chosen value of 50,000 J·mol^{-1} is an arbitrary number to destabilize the monomers and dimers at high BeF_2 concentrations. It is close to the value adopted by Robelin and Chartrand for the CALPHAD model of the NaF-BeF_2 system (49,162 J·mol^{-1}) [34].

The present model includes three excess Gibbs energy expressions for the SNN exchange reactions associated with the formation of the (Li-F-Be_{IV}), (Li-F-Be_2) and (Li-F-Be_3) quadruplets, i.e. $\Delta g_{LiBe_{IV}/F}$, $\Delta g_{LiBe_2/F}$ and $\Delta g_{LiBe_3/F}$.

The selected SNN coordination numbers are listed in Table 4. In the two-sublattice quadruplet approximation of Pelton et al. [40], the ratio between the first-nearest neighbour (FNN) coordination number z_i and the second-nearest neighbour (SNN) coordination number Z_i is constant and equal to:

$$\frac{Z_i}{z_i} = \zeta/2 \tag{14}$$

where ζ was set equal to 2.4 for the reciprocal system {Li, Na, K, Mg, Ca//F, Cl} in Ref. [41]. The same value was adopted by Robelin and Chartrand for the $\{NaF + AlF_3 + CaF_2 + BeF_2 + Al_2O_3 + BeO\}$ system [34], and was retained here. Considering four first-nearest neighbours for beryllium as confirmed by the molecular dynamics simulations [25,26], the coordination numbers $Z^{Be_{IV}}_{Be_{IV}Be_{IV}/F_2}$, $Z^{Be_{IV}}_{Be_{IV}Be_2/F_2}$, and $Z^{Be_{IV}}_{Be_{IV}Be_3/F_2}$ are set equal to 4.8. Note also the choice of $Z^{Be_{IV}}_{LiBe_{IV}/F_2} = 3\ Z^{Li}_{LiBe_{IV}/F_2}$, $Z^{Be_2}_{LiBe_2/F_2} = 4\ Z^{Li}_{LiBe_2/F_2}$, and $Z^{Be_3}_{LiBe_3/F_2} = 4\ Z^{Li}_{LiBe_3/F_2}$ which corresponds to maximum short-range ordering near the compositions $x(BeF_2) = 0.25$ ("Li_3BeF_3"), $x(BeF_2) = 0.333$ (Li_2BeF_4), and $x(BeF_2) = 0.43$ ("$Li_4Be_3F_{10}$"). This choice of cation-cation coordination numbers ratios was found to best reproduce simultaneously (i) the distribution of beryllium species across the full range of composition as calculated by the MD simulations (see Section 4.1.3); (ii) the phase diagram data by Refs. [7-9]; (iii) the enthalpy of mixing data measured experimentally by Ref. [10] and calculated from the MD simulations (see Section 4.1.4).

All the ternary subsystems of the LiF-"BeF_2" binary system need to be defined as either "symmetric" or "asymmetric", according to the description in Ref. [42]. The subsystems $\{LiF + Be_{IV}F_2 + Be_2F_4\}$, $\{LiF + Be_{IV}F_2 + Be_3F_6\}$, and $\{LiF + Be_2F_4 + Be_3F_6\}$ are all three asymmetric with LiF as the asymmetric component, while the system $\{Be_{IV}F_2 + Be_2F_4 + Be_3F_6\}$ is symmetric. Accordingly, the composition dependence for the quadruplets as a function of the cation-cation pair mole fractions becomes:

$$\chi_{LiBe_{IV}/F_2} = \chi_{LiBe_2/F_2} = \chi_{LiBe_3/F_2} = \frac{X_{LiLi}}{\sum_k \sum_{l \gg k} X_{kl/F_2}} \tag{15}$$

$$\chi_{Be_{IV}Li/F_2} = \chi_{Be_2Li/F_2} = \chi_{Be_3Li/F_2} = \frac{X_{Be_{IV}Be_{IV}} + X_{Be_2Be_2} + X_{Be_3Be_3} + X_{Be_{IV}Be_2} + X_{Be_{IV}Be_3} + X_{Be_2Be_3}}{\sum_k \sum_{l \gg k} X_{kl/F_2}} \tag{16}$$

where k and l represent the Li^+, Be_{IV}^{2+}, Be_2^{4+}, and Be_3^{6+} cations. In the case of the {LiF + "BeF_2"} system, $\sum_k \sum_{l \gg k} X_{kl/F_2} = 1$.

The optimized Gibbs energies for the second-nearest neighbours exchange reactions are finally:

$$\Delta g_{LiBe_{IV}/F_2}/(\mathrm{J{\cdot}mol^{-1}}) = -21{,}500 - 9(T/K) + 1000\,\chi_{LiBe_{IV}/F_2} \tag{17}$$

$$\Delta g_{LiBe_2/F_2}/(\mathrm{J{\cdot}mol^{-1}}) = -37{,}500 - 5(T/K) \tag{18}$$

$$\Delta g_{LiBe_3/F_2}/(\mathrm{J{\cdot}mol^{-1}}) = -12{,}000 - 23(T/K) + (22{,}000 - 21(T/K))\chi_{Be_3Li/F_2} + 9900\,\chi^2_{Be_3Li/F_2} \tag{19}$$

These were obtained by fitting simultaneously (i) the distribution of $[BeF_4^{2-}]$, $[Be_2F_7^{3-}]$ and $[Be_3F_{10}^{4-}]$ units as calculated from the MD simulations, (ii) mixing enthalpy data derived experimentally [10] and from MD simulations, (iii) experimental phase diagram data [7-9], (iv) experimental activity data [11,43,44].

3.3. Gas phase

The gas phase is described by an ideal mixture of (LiF, Li_2F_2, Li_3F_3, $LiBeF_3$, BeF_2, Be_2F_4) gaseous species. The Gibbs energy functions for the gaseous species were taken from the JANAF tables and Ref. [34] and are listed in Table 3 with the corresponding references.

4. Results and discussion

4.1. Thermo-physical properties derived from MD simulations

4.1.1. Density and molar volume

The density of the salt mixtures was calculated for each composition and temperature based on the mean volume of the cubic simulation cell after the 500 ps equilibration in the NPT ensemble at 0 GPa. The results, converted to the molar volumes, are shown in Fig. 2, in which they are compared to the data at $T = 873$, 973, 1073 K of Blanke et al. who measured for $x(BeF_2) = 0$–0.55 [45] and Cantor et al. who measured for $x(BeF_2) = 0.502$, 0.749, 0.892 [15]. The agreement is rather good.

The results for the $x(BeF_2) = 0.33$, 0.5, and 0.75 compositions as a function of temperature are moreover compared to the experimental data of Cantor et al. obtained for mixtures with composition $x(BeF_2) = 0.34$ [16], $x(BeF_2) = 0.502$, 0.749 [15], and the data of Blanke et al. obtained for compositions $x(BeF_2) = 0.3333$, 0.5 [45]. The simulations seem to underestimate slightly the densities, the deviation with the data of Cantor et al. [15,16] being of the order of ~0.6%, 1.5% and 3.9% for the $x(BeF_2) = 0.33$, 0.5, and 0.75 compositions, respectively, but the overall agreement is good. The evolution

Table 4
Cation-cation coordination numbers of the liquid solution.

k	l	Z^k_{kl/F_2}	Z^l_{kl/F_2}	Z^F_{kl/F_2}
Li	Li	6	6	6
Be_{IV}	Be_{IV}	4.8	4.8	2.4
Be_2	Be_2	6	6	1.5
Be_3	Be_3	6	6	1
Be_{IV}	Be_2	4.8	6	1.85
Be_{IV}	Be_3	4.8	6	1.41
Be_2	Be_3	6	6	1.2
Li	Be_{IV}	2	6	2.4
Li	Be_2	1.5	6	1.5
Li	Be_3	1.5	6	1.2

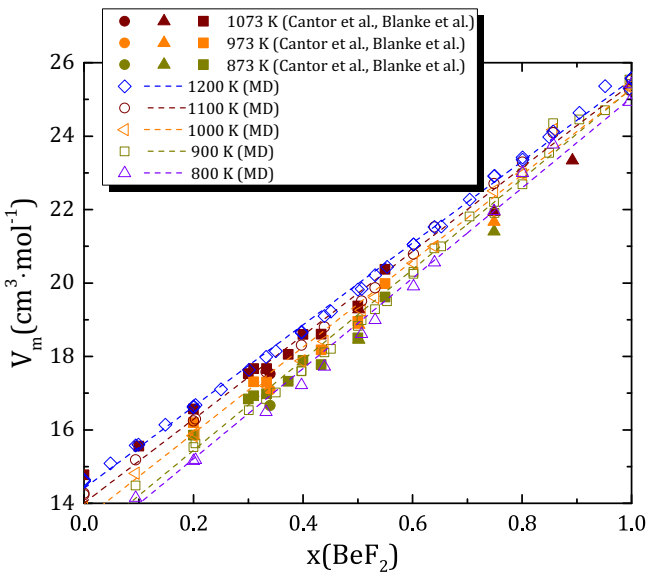

Fig. 2. Molar volume of (Li,Be)F$_x$ melt at $T = 800, 900, 1000, 1100, 1200$ K compared to the data of Blanke et al. [45] (■) and Cantor et al. [15] (▲), [16] (●) measured at $T = 873, 973, 1073$ K.

of both the densities and molar volumes are linear with temperature (see Fig. 3), and the fitting equations for all compositions are summarized in Table 5.

The evolution of the density as a function of composition is depicted in Fig. 4 for $T = 800, 900, 1000, 1100, 1200$ K. Interestingly, the density at those temperatures shows a maximum around $x(BeF_2) \sim 0.3$–0.45, which can be related to the local structure of the melt (Section 4.1.3). The same feature is seen when plotting the excess molar volume (Fig. 4b), which shows an S-shape curve, with a maximum of the negative deviation from the ideal behaviour around $x(BeF_2) \sim 0.4$, and a slightly positive deviation at high BeF$_2$ concentrations. The $x(BeF_2) \sim 0.3$–0.45 composition range corresponds to

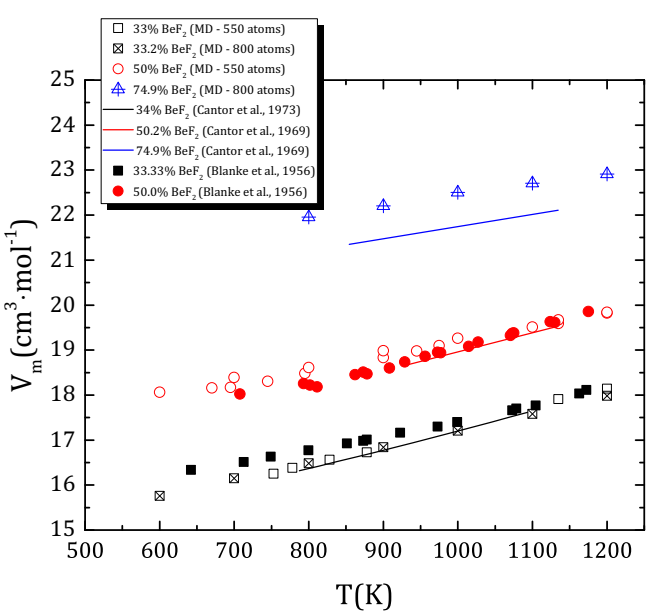

Fig. 3. Comparison of the simulation results at $x(BeF_2) = 0.343$, 0.5, 0.749 with experimental molar volumes reported on (Li,Be)F$_x$ molten mixtures at compositions $x(BeF_2) = 0.34$ [16], $x(BeF_2) = 0.502, 0.749$ [15], and $x(BeF_2) = 0.3333, 0.5$ [45].

Table 5
Linear evolution of the molar volume versus temperature as obtained by fitting of the simulation results.

$x(BeF_2)$	V_m (cm^3·mol^{-1})	T (K)
0	10.425 + 3.48·10^{-3}T	700–1200
0.094	11.290 + 3.55·10^{-3}T	800–1200
0.2–0.203	12.285 + 3.62·10^{-3}T	600–1200
0.33–0.332	13.549 + 3.65·10^{-3}T	600–1200
0.397	14.434 + 3.48·10^{-3}T	700–1200
0.439	15.077 + 3.36·10^{-3}T	700–1200
0.5–0.507	16.099 + 3.10·10^{-3}T	600–1200
0.532	16.552 + 3.04·10^{-3}T	700–1200
0.602	17.707 + 2.80·10^{-3}T	800–1200
0.640	18.707 + 2.41·10^{-3}T	700–1200
0.749	20.049 + 2.41·10^{-3}T	800–1200
0.801	21.329 + 1.81·10^{-3}T	900–1200
1	24.982 + 4.947·10^{-4}T	600–1200

the transition region from a molecular type of liquid including BeF_4^{2-}, Li^+ and F^- (predominant) species to a polymeric type of liquid with the formation of dimers, trimers, and higher order polymeric units with increasing BeF$_2$ content. An S-shape curve is also observed for the enthalpy of mixing as described in detail in Section 4.1.4. The positive contribution at high BeF$_2$ concentration was attributed to the breakdown of the three-dimensional network structure of beryllium fluoride by addition of the alkali cation [10]. The same interpretation fits with the evolution of the excess molar volume calculated by MD.

4.1.2. Thermal expansion

The thermal expansion β of the (Li,Be)F$_x$ melt was subsequently derived from the simulation results as a function of temperature from the relation:

$$\beta = -\frac{1}{\rho}\left(\frac{\partial \rho}{\partial T}\right)_p \quad or \quad \beta = \frac{1}{V_m}\left(\frac{\partial V_m}{\partial T}\right)_p \tag{20}$$

The variation is quasi-linear with temperature (Fig. 5) and the fitting equations for each composition are listed in Table 6. It is interesting the compare those data with the results obtained in the same temperature range for NaF-ZrF$_4$ and LiF-NaF-KF melts by Salanne et al. [4]. The thermal expansion of the fully ionic liquid (LiF:NaF:KF) = (0.465:0.115:0.42) is the highest (in the order of 3.2 –3.6·10^{-4} K^{-1}), followed by (NaF:ZrF$_4$) = (0.57:0.43) (in the order of 2.9 –3.2·10^{-4} K^{-1}), and then LiF-BeF$_2$ (in the order of 0.5 –2.5·10^{-4} K^{-1} depending on composition, as shown in Fig. 5). The (Na,Zr)F$_x$ melt is characterized by the co-existence of molecular complexes ZrF_6^{2-}, ZrF_7^{3-}, and ZrF_8^{4-}, which can moreover be linked to each other with a bridging fluorine [46]. It is hence seen that the more the melt is structured at the molecular level by strong bonds resulting in long-range order, the smaller is the corresponding thermal expansion.

4.1.3. Local structure

Previous molecular dynamic studies on this system by Salanne et al. [26,27] have shown that the (Li,Be)F$_x$ melt is made of a network of tetrahedral corner-sharing Be^{2+} cations linked by F^- anions, whereas Li^+ cations do not form any particular complex. At low BeF$_2$ content, the melt is essentially well-dissociated and is constituted of Li^+, BeF_4^{2-}, and F^- species. Polymeric species such as $Be_2F_7^{3-}$, $Be_3F_{10}^{4-}$, $Be_4F_{13}^{5-}$, etc. are moreover formed progressively, when the BeF$_2$ concentration increases, until a fully connected network is obtained for pure BeF$_2$, similar to the tetrahedral network of silica SiO$_2$.

The exact chemical speciation as a function of temperature and composition can be extracted from the MD simulations by identifying Be^{2+} cations with common F^- anions in their coordination shells. The radial distribution function (RDF) of the F^- anions around the Be^{2+} cations is calculated (see example in Fig. 6), and the first local

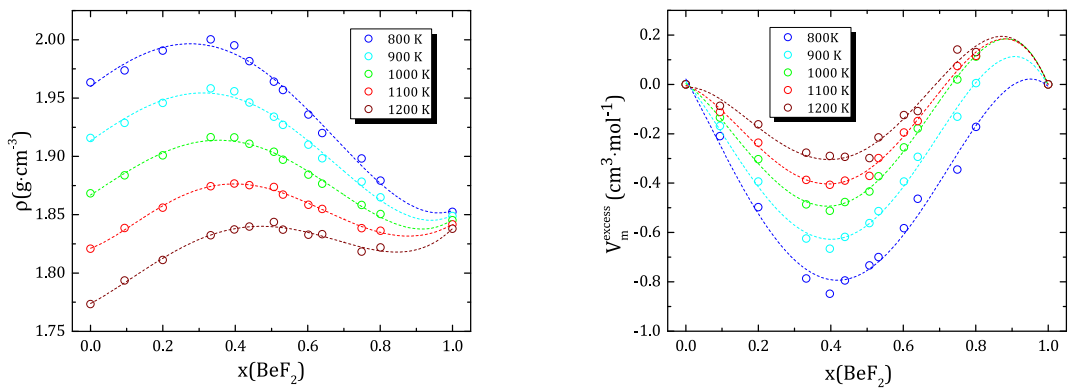

(a) ρ (b) V_m^{excess}

Fig. 4. Evolution of the (a) density and (b) excess molar volume as a function of temperature and composition as derived from the MD simulations.

minimum is assigned to the bond cut-off distance. Any anion closer to the cation than the minimum of the RDF is said to belong to the first coordination shell. In Fig. 6, the Be-Be RDF, calculated for the $x(BeF_2) = 0.5$ composition at $T = 1135$ K, shows a rather sharp peak with a maximum at a distance of 3.03 Å. The latter distance is less than two Be-F distances (at 1.57 Å), indicating a Be-F-Be linkage. Applying this procedure to describe the linkages in the melt, the chains of connected Be^{2+} cations are identified.

The result of this analysis performed in this work at $T = 900$, 1000, 1100, 1135 and 1200 K are shown in Figs. 7 and B.2. The output of the simulations can be expressed as percentage of F atoms or Be atoms involved in the various species. The calculated data at $T = 1200$ K are in excellent agreement with the results of Refs.[26,27], while the speciation at the other temperatures are reported for the first time. These calculations are used as input for the optimization of the coupled structural-thermodynamic model for this system as explained in Section 4.2. Note that in the MD simulations, the "polymer" corresponds to all clusters with a Be nuclearity greater than 4. For the purpose of the CALPHAD modelling, "$Be_3F_{10}^{4-}$" is assumed to represent the largest possible polymeric species, i.e. includes the $Be_3F_{10}^{4-}$ units plus all clusters with a Be nuclearity greater than 3.

4.1.4. Thermodynamic properties

Some key thermodynamic properties, i.e. enthalpy and heat capacity, can be derived from the molecular dynamic simulations.

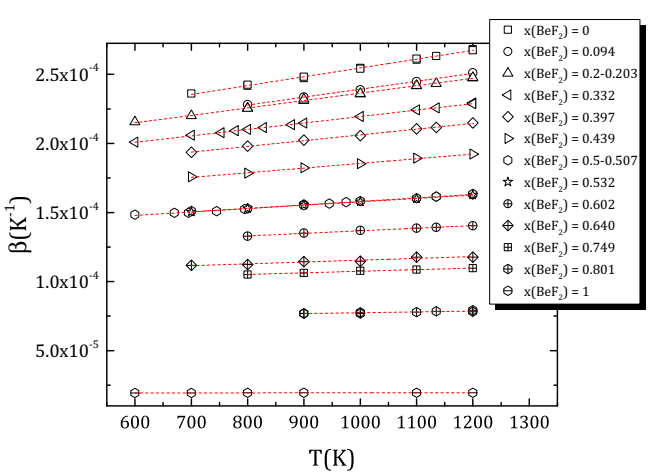

Fig. 5. Thermal expansion of the (Li,Be)F_x melt as derived from the MD simulations.

The enthalpy is obtained directly from the (average) potential energy of the 1 ns production run in the NPT ensemble. The evolution of the molar enthalpies as a function of temperature and composition is shown in Fig. 8.

By performing simulations at a fixed temperature while varying the composition, the enthalpies of mixing $\Delta_{mix}H_m^o$ can moreover be computed, as done in this work at $T = 700$, 800, 900, 1000, 1100, 1135 and 1200 K:

$$\Delta_{mix}H_m^o = H_m^o(T) - [1 - x(BeF_2)]H_m^o(LiF, T) - x(BeF_2)H_m^o(BeF_2, T) \quad (21)$$

The results are shown in Fig. 9 and compared to the experimental data of Holm and Kleppa [10] measured at $T = 1135$ K by high-temperature reaction calorimetry. The peculiar S-shape of the enthalpy curve is well-reproduced in the MD simulations, with positive values for high BeF_2 content, although the overall trend is more negative. The simulations also show that the mixing enthalpy tends to more negative values as the temperature is decreased. The S-shape and therefore strong energetic asymmetry in this system was related to the breakdown of the network structure of liquid BeF_2 in the study by Holm and Kleppa [10]. This interpretation is in accordance with the findings of the MD simulations: when LiF is added to the BeF_2 liquid, the 3-dimensional polymeric network is progressively disrupted and the Be-F-B bridging bonds are broken, which results in a positive contribution to the enthalpies of mixing and excess molar volume as seen previously. The minimum in the enthalpy of mixing curves moreover occurs around $x(BeF_2)$ ~0.3 –0.4, which can be related to the increasing stability of the BeF_4^{2-} anionic complexes.

Table 6
Thermal expansion versus temperature of the (Li,Be)F_x melt as obtained by fitting of the simulation results.

$x(BeF_2)$	β (K^{-1})	T (K)
0	$1.909 \cdot 10^{-4} + 6.375 \cdot 10^{-8}T$	700–1200
0.094	$1.820 \cdot 10^{-4} + 5.726 \cdot 10^{-8}T$	800–1200
0.2–0.203	$1.827 \cdot 10^{-4} + 5.377 \cdot 10^{-8}T$	600–1200
0.33–0.3323	$1.728 \cdot 10^{-4} + 4.666 \cdot 10^{-8}T$	600–1200
0.397	$1.646 \cdot 10^{-4} + 4.163 \cdot 10^{-8}T$	700–1200
0.439	$1.518 \cdot 10^{-4} + 3.379 \cdot 10^{-8}T$	700–1200
0.5–0.507	$1.327 \cdot 10^{-4} + 2.539 \cdot 10^{-8}T$	600–1200
0.532	$1.333 \cdot 10^{-4} + 2.447 \cdot 10^{-8}T$	700–1200
0.602	$1.181 \cdot 10^{-4} + 1.866 \cdot 10^{-8}T$	800–1200
0.64	$1.023 \cdot 10^{-4} + 1.318 \cdot 10^{-8}T$	700–1200
0.749	$9.594 \cdot 10^{-5} + 1.153 \cdot 10^{-8}T$	800–1200
0.801	$7.137 \cdot 10^{-5} + 6.056 \cdot 10^{-9}T$	900–1200
1	$1.912 \cdot 10^{-5} + 3.786 \cdot 10^{-10}T$	600–1200

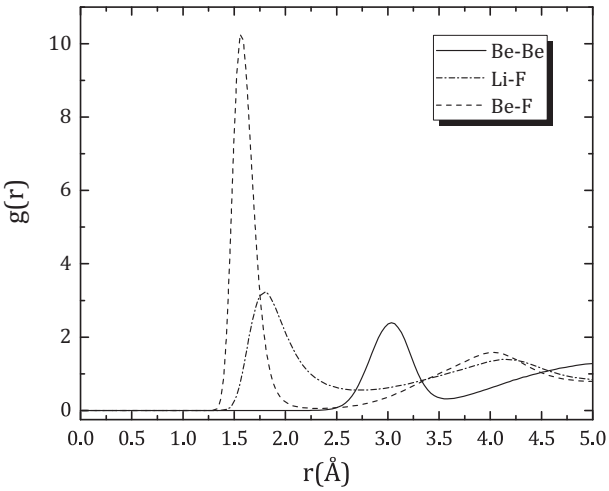

Fig. 6. Radial distribution functions obtained for $x(BeF_2) = 0.5$ at $T = 1135$ K.

The heat capacity is obtained from the average potential energy of the 1 ns NPT simulations run at neighbouring temperatures according to the equation:

$$C_{p,m} = \left(\frac{\partial H_m}{\partial T}\right)_p \tag{22}$$

The variation of the molar enthalpies is linear up to the composition $x(BeF_2) = 0.602$ and was fitted as such in the temperature range 900–1200 K. For the compositions $x(BeF_2) = 0.640$, 0.749, 0.801, 0.857, a fitting with a second order polynomial function seems more appropriate, and was applied in the temperature range 800–1200 K. The fitting equations are shown in detail together with the simulation results in the Appendix (see Fig. C.4). After derivation of those equations, the heat capacity functions were subsequently derived: a constant heat capacity was obtained up to $x(BeF_2) = 0.602$, and a linear heat capacity function was obtained for the more concentrated compositions $x(BeF_2) = 0.640$, 0.749, 0.801, 0.857. The results above $x(BeF_2) = 0.857$ were quite scattered and could not be exploited further for the analysis of the heat capacity. The simulations at very high BeF_2 content appeared very challenging due to the formation of the three-dimensional polymeric network and long polymeric chains, which requires large simulation cells and long simulation times to yield reliable results.

The heat capacity determined at $T = 900$, 1000, 1100 and 1200 K from the simulations are shown in Fig. 10a. The heat capacity derived from the simulations for pure LiF, i.e. 66.6 $J \cdot K^{-1} \cdot mol^{-1}$ is 1.6% higher than the experimental value recommended in the literature, i.e. 64.183 $J \cdot K^{-1} \cdot mol^{-1}$ [33]. Experimental measurements of the heat capacity of molten $(Li,Be)F_x$ have been reported at the composition $x(BeF_2) = 0.34$ by Hoffman and Cooke (79.77 $J \cdot K^{-1} \cdot mol^{-1}$, unknown temperature range, cited in Cantor et al. [13]) and Douglas and Payne [14] (78.45 $J \cdot K^{-1} \cdot mol^{-1}$ in the temperature range 773–873 K). The data obtained with the simulations at $x(BeF_2) = 0.332$, i.e. 77.72 $J \cdot K^{-1} \cdot mol^{-1}$, are in very good agreement with the latter data. Experimental data for other compositions are not available, but the results of the simulations are also compared in Fig. 10a to the heat capacity data computed from our coupled structural-thermodynamic model presented in the following Section 4.2. The agreement is overall rather good. The heat capacity derived from the simulations is independent of temperature up to $x(BeF_2) = 0.602$, which is not the case in the model, however, in which a temperature dependence exists over the entire composition range. Based on this comparison, one sees that the simulations best represent the heat capacity of the molten salt for a temperature around $T = 1200$ K.

From the simulation results, the excess heat capacity was determined as done previously for the excess molar volume and enthalpies of mixing. One difficulty here is that the simulations could not give a reliable result for the BeF_2 end-member. Taking the same value as in our coupled structural-thermodynamic model at $T = 1200$ K, i.e. $C^o_{p,m}(BeF_2, l, 1200\,K) = 94.91\,J \cdot K^{-1} \cdot mol^{-1}$, one computes the excess heat capacity shown in Fig. 10b. The simulation results seem to reproduce the maximum as predicted in our coupled structural-thermodynamic model around $x(BeF_2) = 0.3$. The comparison is only qualitative and tricky, however, since the result is directly influenced by the choice of the heat capacity of the BeF_2 end-member.

4.1.5. Viscosity

The viscosity of LiF-BeF_2 molten salt mixtures have been measured by several authors, with a very good agreement between the various studies: Cohen and Jones [47] ($x(BeF_2) = 0.31$ at $T = 873$, 973, 1073 K), Abe et al. [48] ($x(BeF_2) = 0.328$ in the range $T = 812.5$ – 1573 K), Blanke et al. [45] ($x(BeF_2) = 0.10$, 0.31, 0.3733, 0.4333, 0.5, 0.55 at $T = 873$, 973, 1073 K), Cantor et al. [15] ($x(BeF_2) = 0.36$–0.99 in the range $T = 649$–1240 K), and Desyatnik et al. [49] ($x(BeF_2) = 0$, 0.1, 0.2, 0.3, 0.4, 0.4, 0.5, 0.6, 0.7, 0.8, 0.9, 1 in the range $T = 802$–1333 K). Salanne et al. [26] showed that the interaction potentials for the LiF-BeF_2 system yield a good agreement with the experimental data of Cantor et al. [15] across the studied composition range ($x(BeF_2) = 0$–0.55) at $T = 873$ K, with a sharp increase in the viscosity above 33% BeF_2 due to the network formation.

In this work, the viscosity was evaluated for the selected compositions and temperatures by the Green-Kubo method, i.e. by calculating the time integral of the shear stress autocorrelation function:

$$\eta = \frac{V}{k_B T}\int_0^\infty < \sigma_{\alpha\beta}(t) \cdot \sigma_{\alpha\beta}(0) > dt \tag{23}$$

where V is the volume of the simulation cell, k_B the Boltzmann constant, T the temperature, $\sigma_{\alpha\beta}$ one of the components of the stress tensor. To improve the statistics, the stress autocorrelation function is averaged over the five components (σ_{xy}, σ_{xz}, σ_{yz}, σ_{xx-yy}, $\sigma_{2zz-xx-yy}$), and the simulation is run for much longer times (5 to 10–20 ns) to reach a plateau for the running integral. An example of the integration of the shear stress autocorrelation function for $x(BeF_2) = 0.33$ at $T = 1100$ K is shown in the Supplementary materials. A test was performed with 20 ns for pure BeF_2, but the plateau could not be reached in this highly polymerized system, even for such long simulation times (see Supplementary materials). Hence, only limited results at the highest temperatures were obtained for high BeF_2 concentrations.

The results of the simulations at $x(BeF_2) = 0.2$, 0.203 and 0.332 in the temperature range 600–1200 K are compared in Fig. 11 to the experimental data of Blanke et al. [45] and Cohen and Jones [47] obtained for the composition $x(BeF_2) = 0.31$, and to the data of Abe et al. [48] obtained for $x(BeF_2) = 0.328$. The agreement is reasonably good, although the MD simulations seem to slightly overestimate the viscosity compared to the literature data. One should point out, however, the difficulty in performing the measurements on those highly corrosive and hygroscopic materials on the one hand, and the challenges in assessing properly those physico-chemical properties in a highly polymerized system such as LiF-BeF_2 on the other hand (requiring very large simulation boxes and long simulation times).

The simulation results at $T = 900$, 1000, 1100 K are moreover compared in Fig. 12 to the experimental data of Cantor et al. [15] in the range $x(BeF_2) = 0.36$ –0.99, and Desyatnik et al. [49] in the

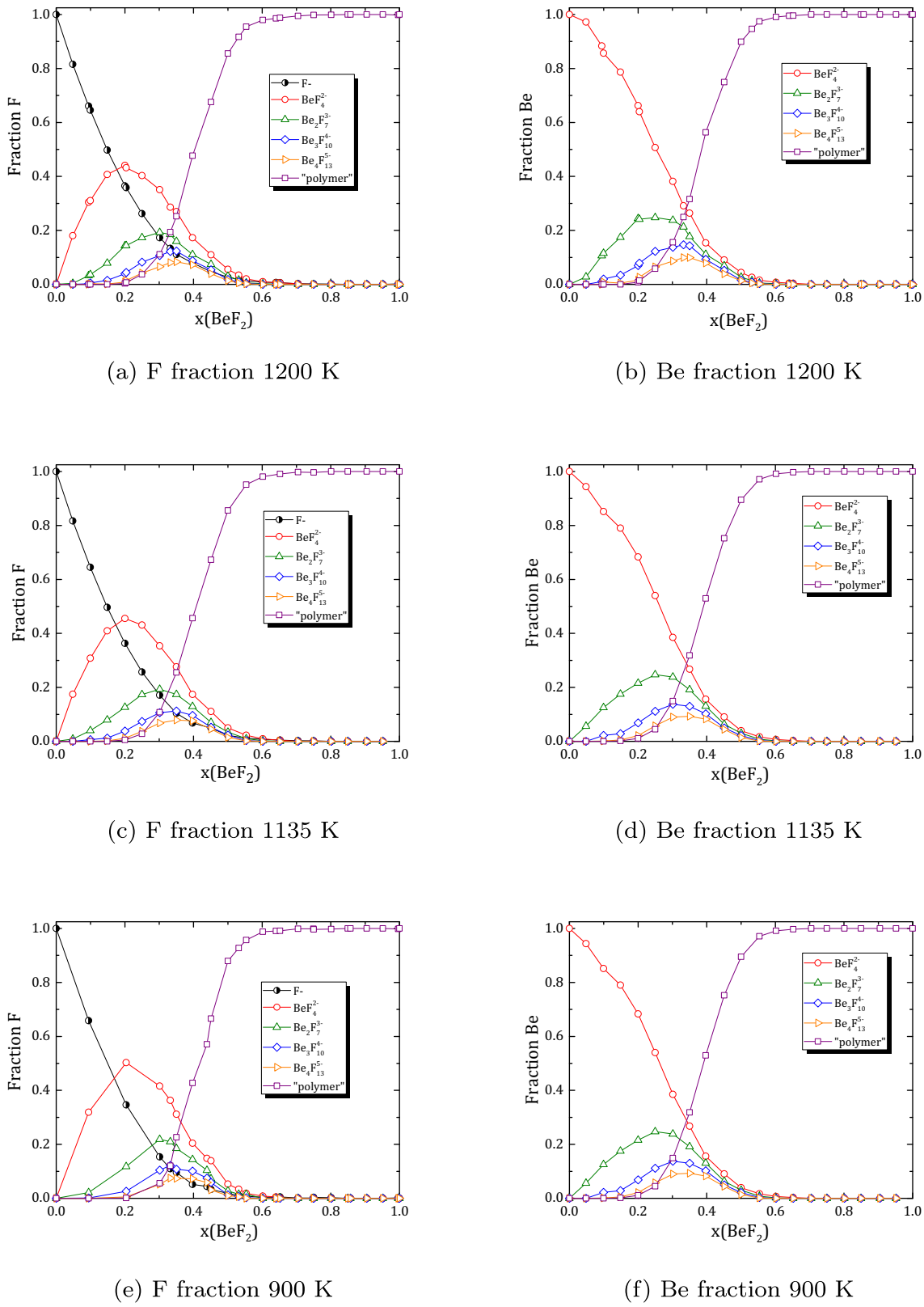

Fig. 7. Fraction of F atoms and Be atoms involved in various species observed in the system as a function of composition at $T = 900, 1135, 1200$ K; "polymer" means a cluster with a Be nuclearity greater than 4, whereas F^- implies that the ion is coordinated only to Li^+.

range $x(BeF_2) = 0$–1, interpolated at those temperatures (by applying the Arrhenius correlation as listed by the authors). The general agreement is very good.

The evolution of the viscosity as a function of temperature is shown in Fig. 13a, together with the Arrhenius fit to the simulation results. A steep increase in the viscosity is observed with decreasing

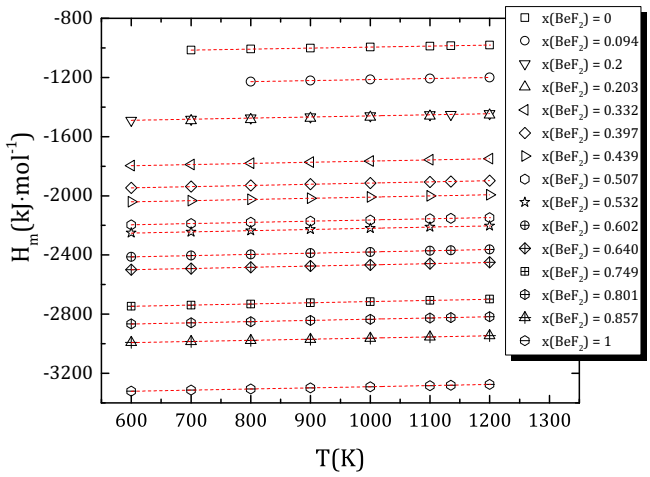

Fig. 8. Evolution of the molar enthalpies of the (Li,Be)F_x melt as a function of temperature.

temperature and increasing BeF_2 concentration, as expected. The least-square fitted parameters for a simple Arrhenius equation of the form $\eta = A\exp(E_n/RT)$ are listed in Table 7. The evolution of the fitted activation energy for viscous flow E_n is displayed in Fig. 13b, which shows a steep increase with increasing BeF_2 content, again related to the formation of polymeric units.

4.1.6. Thermal conductivity

Similarly to the viscosity, the thermal conductivity is obtained via the Green-Kubo formalism by integration of microscopic fluxes autocorrelation functions, $L_{\alpha\beta}$, defined as:

$$L_{\alpha\beta} = \lim_{\tau\to\infty}\left[\frac{1}{3k_BT}\int_0^{\tau}\langle \mathbf{J}_\alpha(t)\cdot\mathbf{J}_\beta(t)\rangle dt\right] \tag{24}$$

where α and β take the values of either e or z_i, k_B and V being the Boltzmann constant and the equilibrium volume, respectively. $\mathbf{J}_e$ and $\mathbf{J}_{z_i}$ represent the energy flux and the charge flux of the i-th

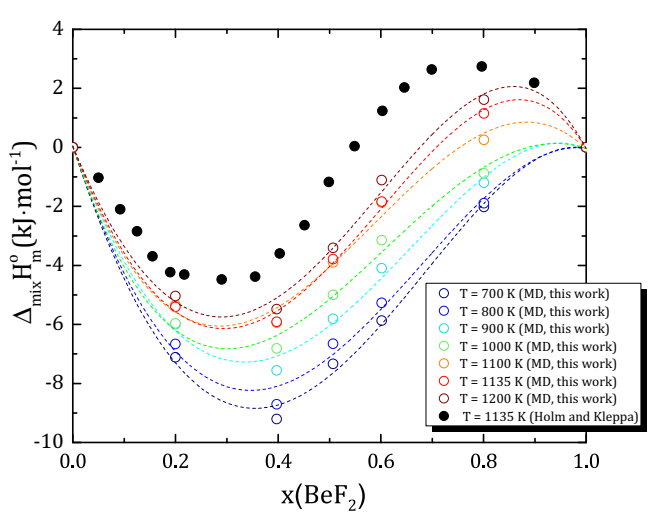

Fig. 9. Enthalpies of mixing calculated from the MD simulations at $T = 700$, 800, 900, 1000, 1100, 1135 and 1200 K, and comparison with the experimental data of Holm and Kleppa [10] measured at $T = 1135$ K.

Table 7
Evolution of viscosity versus composition as obtained by fitting of the simulation results with a simple Arrhenius equation of the form $\eta = A\exp(E_n/RT)$.

$x(BeF_2)$	η(cP) = $A\exp(E_n/RT)$	
	A	E_n (J·mol^{-1})
0	0.16195	23,926
0.094	0.10441	28,942
0.2–0.203	0.09012	28,638
0.332	0.05624	38,765
0.397	0.02421	45,680
0.439	0.09285	37,958
0.507	0.08412	41,227
0.532	0.02866	52,059
0.602	0.00714	65,527

ion, respectively. From these fluxes autocorrelation functions, the thermal conductivity is given by:

$$\lambda(T) = \frac{1}{T^2}\left[L_{ee}(T) - \frac{L_{ez}^2(T)}{L_{zz}(T)}\right] \tag{25}$$

for a single compound and

$$\lambda(T,x) = \frac{1}{T^2}\left[L_{ee}(T,x) - \frac{A(T,x)}{B(T)}\right] \tag{26}$$

for a binary mixture, with $A = L_{ez_1}^2 L_{z_2z_2} + L_{ez_2}^2 L_{z_1z_1} - 2L_{ez_1}L_{ez_2}L_{z_1z_2}$ and $B = L_{z_1z_1}L_{z_2z_2} - L_{z_1z_2}^2$.

The simulations results for pure LiF are compared in Fig. 14 with the estimated data of Ref. [50], experimental data of Refs. [51-55], molecular dynamics data of Refs.[56,57], and the model of Gheribi et al. predicting the thermal conductivity of pure alkali and alkaline-earth salts [58]. The scatter in the experimental data is quite large, mainly due to problems of heat transfer mechanisms (convection and radiation), purity and homogeneity of samples as discussed in Refs.[58,59]. The most reliable and accepted experimental data are marked with a "R" in Fig. 14. The estimated values of Nagasaka and Nagashima [50] are also considered sound in the literature [60]. In any case, a negative temperature dependence is expected for the thermal conductivity [58,59] as discussed by DiGuilo [61]. This is indeed the case in our predictions from the polarizable interaction potentials, but the deviation with the recommended data is about 30%. This is a general feature observed for molecular dynamics simulations on such fully dissociated ionic systems [60]. The results of Refs.[56,57] for LiF shown in Fig. 14 are also about 30% too high. This overestimation by MDs is moreover correlated to the mass of the alkali cation as evident from the results along the LiF-NaF-KF-RbF-CsF series reported in Ref. [58]. The simulations give better results for the heavier alkali metals.

In Fig. 15, the results for all compositions are shown for $T = 800$, 900, 1000, 1100, 1200 K. The predicted values from the model of Gheribi et al. [58] for pure LiF and BeF_2 are also displayed at $T = 800$ and 1200 K. The latter model requires only input on density, heat capacity, velocity of sound and melting temperature, and has shown to give good results on a variety of salts (fluorides, chlorides, bromides, iodides, carbonates, nitrates, nitrites, sulfates, hydroxides), with an estimated accuracy of 20%.

Thermal conductivity and thermal diffusivity measurements were reported in the literature at $x(BeF_2) = 0.34$ by Cooke et al. [17] and at $x(BeF_2) = 0.34$ and 0.47 by Kato et al. [18], respectively. The former authors estimated $\lambda = 1.0\,W\cdot m^{-1}\cdot K^{-1}$ at $T = 923$ K and $1.2\,W\cdot m^{-1}\cdot K^{-1}$ in the range 1023–1133 K. It should be pointed out that these result do not follow the correct dependence with temperature [59]. Kato et al. reported thermal diffusivities between the melting temperature and $T = 873$ K equal to $2.5\cdot10^{-7}\,m^2\cdot s^{-1}$

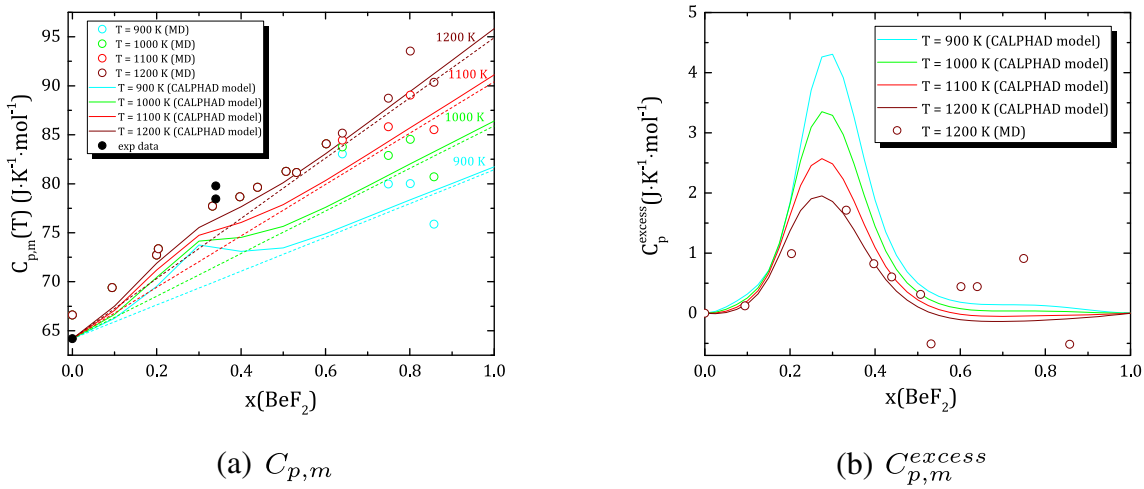

(a) $C_{p,m}$ (b) $C_{p,m}^{excess}$

Fig. 10. (a) Heat capacity and (b) excess heat capacity at $T = 900$, 1000, 1100 and 1200 K of the (Li,Be)F$_x$ liquid solution derived from the MD simulations, and comparison with the heat capacity data computed with our coupled structural-thermodynamic model at the same temperatures. The dotted lines in (a) correspond to an "ideal" heat capacity calculated with the Neumann-Kopp additive rule.

and $2.47 \cdot 10^{-7}$ m^2·s^{-1} for the $x(BeF_2) = 0.34$ and 0.47 compositions, respectively. From those data, we estimated the corresponding thermal conductivities at $T = 800$ K (within their investigated temperature range), by taking the density of the molten salt mixtures from our MD simulations at those compositions (Fig. 4), and the heat capacity computed from our coupled structural-thermodynamic model. The resulting thermal conductivities are 1.103 and 0.971 W·m^{-1}·K^{-1}, respectively, not far from the data of Cooke et al. [17].

The values found in our MD simulations of the mixtures are again somewhat higher. We can assume that the deviation is due mainly to the overestimation of the LiF thermal conductivity for the reasons stated above. We hence propose to correct our MD results with the following equation:

$$\lambda_{corr}(T) = \lambda(T) - 0.384x(LiF) \tag{27}$$

where $\lambda_{corr}(T)$ is the corrected thermal conductivity at temperature T. The value of 0.384 W·m^{-1}·K^{-1} represents the difference between the calculated equilibrium molecular dynamics (EMD) and the experimental thermal conductivity of molten LiF at $T = 1200$ K, i.e. above the melting point (1118 K). This error is quasi constant in the stable liquid region, but increases as the temperature decreases in the undercooled region. Such differences were also observed in other EMD studies [56,57].

The resulting corrected thermal conductivities at $T = 800$ and 1200 K, shown in Fig. 15, are in much better agreement with the literature data and estimated data in the model of Gheribi et al. [60]. The value obtained at $x(BeF_2) = 0.332$ is (1.3 ± 0.2) W·m^{-1}·K^{-1}, slightly higher than the data of Cooke et al. and data derived from the thermal diffusivity measurements of Kato et al., but in very good agreement within uncertainty ranges. The computed data moreover seem to follow an "ideal" linear behaviour (dashed line in Fig. 15), taking the end-members LiF and BeF$_2$ values from the model of Gheribi et al. [60]. In the work of Gheribi and Chartrand [59] on (Li,K)Cl, (Li,Na)Cl, (Na,K)Cl, (Li,K)F, (Li,Na)F and (Na,K)F binary mixtures, a negative deviation from the linear behaviour was reported, where the largest deviation (maximum thermal conductivity degradation) occurred with increasing difference between the ionic radii of the cationic end-members. But the case of (Li,Be)F$_x$ solution, the

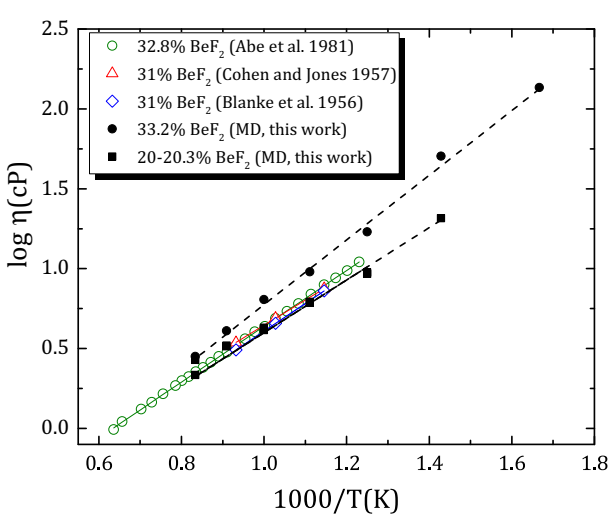

Fig. 11. Comparison of the computed viscosities at $x(BeF_2) = 0.203$ and 0.332 with the experimental data reported by Blanke et al. [45] at $x(BeF_2) = 0.31$, Cohen and Jones [47] at $x(BeF_2) = 0.31$, and Abe et al. [48] at $x(BeF_2) = 0.328$. The straight lines correspond to the Arrhenius fit to the data.

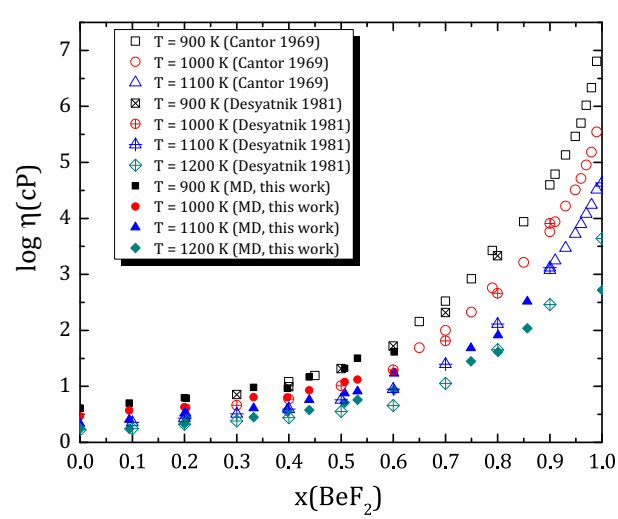

Fig. 12. Comparison of the computed viscosities at $T = 900$, 1000, 1100 K with the data reported by Cantor et al. [15] interpolated at those temperatures.

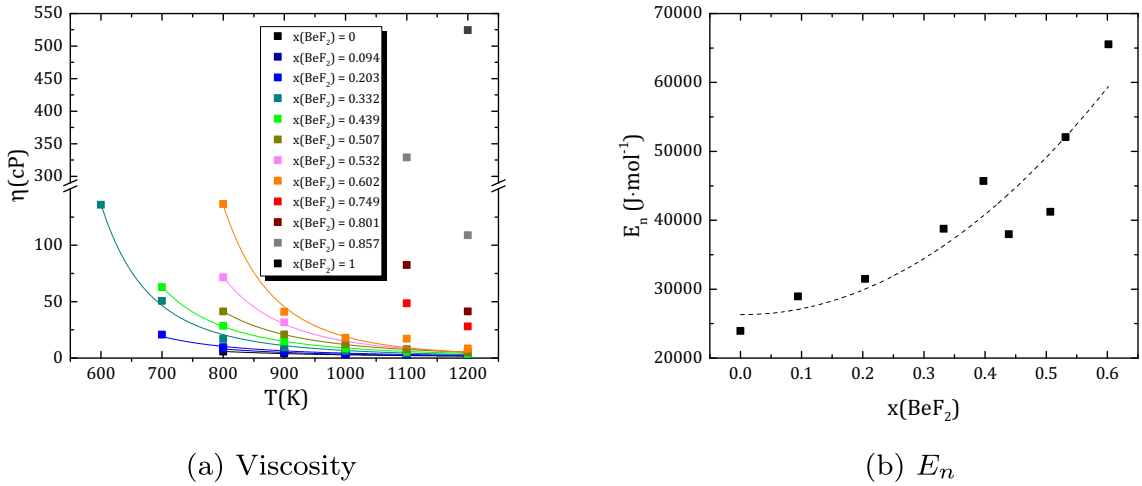

(a) Viscosity (b) E_n

Fig. 13. (a) Computed viscosities at $x(BeF_2) = 0$, 0.094, 0.203, 0.332, 0.397, 0.439, 0.5, 0.532, 0.602, 0.749, 0.801, 0.857, 1 as a function of temperature, and Arrhenius fit to the data (shown as a line). Only the data at the highest temperature $T = 1200$ K were derived for $x(BeF_2) = 1$. (b) Evolution of the fitted activation energy for viscous flow E_n, when fitting the MD results with a simple Arrhenius equation of the form $\eta = A\exp(E_n/RT)$.

mass fluctuation term is small (12.9 g·atom^{-1}·mol^{-1} for LiF and 15.7 g·atom^{-1}·mol^{-1} for BeF_2), which explains the linear behaviour.

4.2. Coupled structural and thermodynamic model of the LiF-BeF_2 system

The agreement between computed thermo-physical properties with the polarizable ionic interaction potentials and the available experimental data is generally very good as seen previously. The MD simulations are not able to give information on chemical equilibrium, however [28]. In particular, entropy data cannot be extracted by MD, which characterizes the properties of a system in a given single state [28]. This means that the Gibbs energy is also not directly obtainable by this method. For a thorough safety assessment of the MSR, the simulation codes used to predict the thermo-physical properties and behaviour of the liquid fuel during normal operation and accidental conditions should also characterize the phase equilibria of the system, however. To this end, we integrate in this work the output of the MD simulations (more specifically the calculated distribution of beryllium species in the melt and the calculated mixing enthalpy) together with the available experimental data, to develop a thermodynamic model for this system based on the CALPHAD methodology and the formalism described in Section 3.

The present CALPHAD model reproduces well the experimental phase diagram and thermodynamic data available on this system in the literature: (i) phase diagram equilibrium data by Roy et al. [7], Thoma et al. [8], and Romberger et al. [9], (ii) enthalpies of mixing of the (Li,Be)F_x liquid solution by Holm and Kleppa [10], (iii) fusion enthalpy of LiF and BeF_2 [33], (iv) activity coefficients of LiF and BeF_2 species measured in the liquid by Hitch and Baes [11], Büchler and Stauffer [43] and Fukuda et al. [44], (v) vapour pressure data by Refs. [43, 44, 62-65]. In addition, a physical description of the liquid is proposed, where the distribution of beryllium species derived from the MD simulations are well followed.

The phase diagram calculated herein is shown in Fig. 16 and compared with the equilibrium data reported in the literature

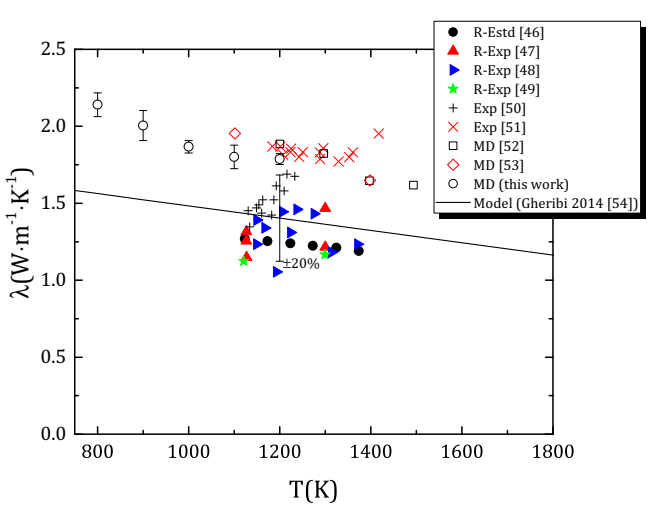

Fig. 14. Computed thermal conductivity of LiF as a function of temperature, compared to the estimated data of Ref. [50], experimental data of Refs. [51-55], molecular dynamics results of Refs. [56, 57], and model of Ref. [58]. More reliable data are identified by "R" in the legends.

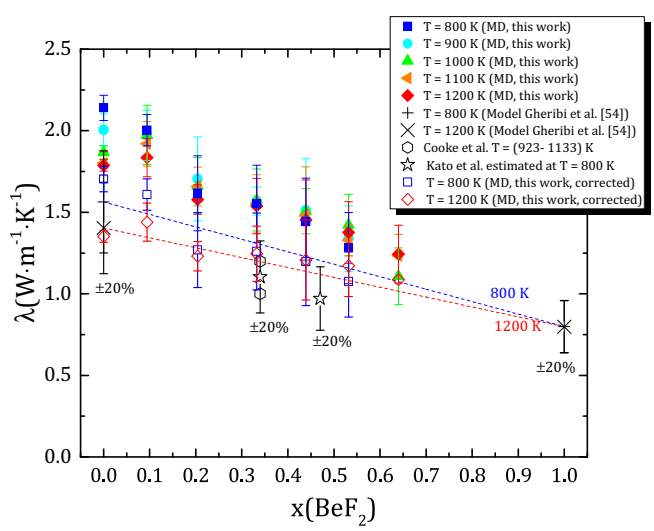

Fig. 15. Computed thermal conductivity at $x(BeF_2) = 0$, 0.094, 0.203, 0.332, 0.439, 0.532, 0.640 as a function of temperature. Comparison with the thermal conductivity data of Cooke et al. [17] and Kato et al. [18] (estimated in this work from the thermal diffusivity data).

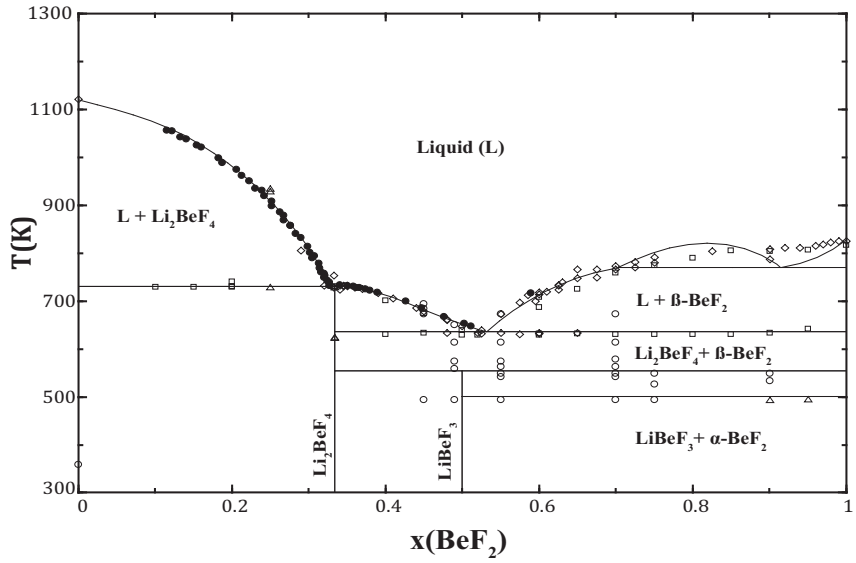

Fig. 16. Calculated LiF-BeF_2 phase diagram and comparison with the experimental data by Roy et al. (1950) [6] (□); Roy et al. (1954) [7]: quenching (○) and DTA (△); Thoma et al. (1968) [8] (◇); and Romberger et al. (1972) [9] (•).

(Table 8), with good agreement. LiF and BeF_2 melt at 1119.5 and 827.4 K, respectively. Two eutectic invariant equilibria are computed at {$T = 730.2$ K and $x(BeF_2) = 0.328$}, and $T = 635.4$ K and $x(BeF_2) = 0.531$, respectively}. Li_2BeF_4 melts congruently at $T = 730.3$ K, while $LiBeF_3$ decomposes into {$Li_2BeF_4(cr) + BeF_2(cr, \beta)$} at $T = 553.8$ K. The computed enthalpy and entropy of fusion for the intermediate compound Li_2BeF_4 are 15.2 kJ·mol^{-1} and 20.8 J·K^{-1}·mol^{-1} at $T_{fus} = 730.15$ K. There are no reference data in the literature for this compound.

Note that only the standard entropies of the intermediate compounds Li_2BeF_4 and $LiBeF_3$ were slightly adjusted compared to the data selected by NIST-JANAF [33] (130.583 and 89.245 J·K^{-1}·mol^{-1}, respectively) to reproduce the reported melting and decomposition temperatures. Moreover, the existence of a miscibility gap was predicted by Vallet and Braunstein [12] in the BeF_2 rich corner of the LiF-BeF_2 system at the critical temperature $T = 807$ K and $x(BeF_2) = 0.781$ based on the extrapolated activity coefficient data of Hitch and Baes [11] and using the Cook-Hilliard method to compute the binodal and spinodal curves. The thermodynamic assessments by Van der Meer using Redlich-Kister polynomials [20], by Beneš and Konings [21] using the modified quasi-chemical model based on the quadruplet approximation and the "structural" thermodynamic model by Romero-Serrano et al. [22] also reproduced this miscibility gap. As pointed out by the authors, a satisfactory agreement between the (i) liquidus data, (ii) the well-known thermodynamic data on BeF_2 and (iii) the model can only be obtained when allowing for the formation of this miscibility gap since the limiting slope of the liquidus curve in the BeF_2 rich corner is related to the fusion enthalpy and fusion entropy of BeF_2 as follows:

$$\lim_{x \to 1} \left(\frac{dT}{dx} \right) = \frac{RT_{fus}^2}{\Delta_{fus} H_m^o} = \frac{RT_{fus}}{\Delta_{fus} S_m^o} \tag{28}$$

In the present model, the miscibility gap is again reproduced. The miscibility gap is imposed by the small fusion entropy of BeF_2

Table 8
Invariant equilibrium points for the LiF-BeF_2 system calculated in the present model and compared to experimental data.

Equilibrium	Invariant reaction	x(BeF_2)	T (K)	Reference
Congruent melting	LiF ⇌ Liq.	0	1119.5	This work (calc.)
		0	(1121 ± 1)	[32]
Eutectic	Liq. ⇌ LiF + Li_2BeF_4	0.328	730.2	This work (calc.)
		–	729	[6]
		0.3280 ± 0.0004	(731.9 ± 0.2)	[9]
Eutectic	Liq. ⇌β-BeF_2 + Li_2BeF_4	0.531	635.4	This work (calc.)
		0.52	629	[6]
		–	621–623	[7]
		0.52	633	[8]
		0.531 ± 0.002	636.5 ± 0.5	[9]
Congruent melting	Li_2BeF_4⇌ Liq.	0.333	730.3	This work (calc.)
		0.333	(731 ± 5)	[6]
		0.333	728	[7]
		0.333	(732.1 ± 0.2)	[9]
		0.333	732.2	[33]
Peritectic	Li_2BeF_4⇌ Liq. + LiF	0.34	731	[8]
Peritectoid	$LiBeF_3 = Li_2BeF_4 + \beta$-$BeF_2$	0.5	553.8	This work (calc.)
		0.5	(573 ± 5)	[7]
		0.5	553	[8]
Congruent melting	BeF_2⇌ Liq.	1	827.4	This work (calc.)
		1	(828 ± 5)	[32]

($5.4\,J\cdot K^{-1}\cdot mol^{-1}$) as discussed by Van der Meer et al. [20]. The temperature of the monotectic equilibrium reaction is $T = 769.2$ K, and the critical temperature and composition {$T = 820.5$ K and $x_{BeF_2} = 0.819$}, are slightly different from the calculated critical point by Vallet and Braunstein [12].

The enthalpy of mixing curve for the (Li,Th)F_x liquid solution calculated with the present model is compared in Fig. 17a with the experimental data by Holm and Kleppa [10] and the result of the MD simulations using the Polarizable Ion Model. The computed enthalpy of mixing reproduces the expected S-shape with values in between the experimental and simulated data. The asymmetry in the enthalpy of mixing curve is obtained with the χ_{Be_3Li/F_2} excess term, while excess entropy terms are necessary to reproduce simultaneously the liquidus and enthalpy of mixing data.

The calculated entropy of mixing ($\Delta_{mix}S^o_m$) (including configurational and non-configurational entropy of mixing) and configurational entropy ($\Delta_{conf}S^o_m$) curves at $T = 1000$ K are shown in Fig. 17b. Both curves show an "m-shape" (although not very marked for the total entropy of mixing) related to the short-range ordering. The dip in the configurational entropy curve is located at the highest composition of maximum short-range ordering ($x(BeF_2) = 0.43$). Similar results were obtained for the NaF-BeF_2 system by Robelin and Chartrand [34], with an even more pronounced "m-shape" for both curves and a sharp minimum of the configurational entropy located around the compositions of maximum short-range ordering (Na_2BeF_4 or $x(BeF_2) = 0.33$ and $Na_3Be_2F_7$ or $x(BeF_2) = 0.40$). One should point out that the latter model included Be^{2+}_{IV} and Be^{4+}_2 cations only, and was not coupled to MD simulations. It would be interesting to apply the same approach as adopted here to that system for a more sound comparison since no experimental data are available on entropies of mixing. Fig. 18 shows the calculated activity and activity coefficients for LiF and BeF_2 in the melt, compared to the experimental data of Hitch and Baes [11] obtained in the composition range $x(BeF_2) = 0.3$–0.9 and temperature range $T = 773$–1173 K using electromotive force measurements. The agreement is very good. Both the model and the experimental data show that the LiF-BeF_2 system is non-ideal, with a negative deviation from ideality below about 50% BeF_2 and a positive deviation from ideality above that composition. The energetic asymmetry is again related to the transition between a molecular type of liquid and a fully connected polymeric network as reported previously to explain the S-shape of the mixing enthalpy data and excess molar volume.

The vapour pressure over pure BeF_2 is mainly constituted of BeF_2(g), with negligible amounts of the dimer Be_2F_4(g). The calculated data in the temperature range $T = 850$–1450 K are in good agreement with the experimental measurements of Sense and Stone [62], Greenbaum et al. [63], Hildenbrand et al. [64], and Fukuda et al. [44] using the transpiration, thermogravimetric, Knudsen cell, and torsion effusion techniques (Fig. 19). The enthalpy of vapourization and sublimation computed in the model at 298.15 K, i.e. $\Delta_{vap}H^o_m(BeF_2,\ 298.15\,K) = 225.4\,kJ\cdot mol^{-1}$ and $\Delta_{sub}H^o_m(BeF_2,\ 298.15\,K) = 230.8\,kJ\cdot mol^{-1}$ are only slightly different from the selected data in NIST-JANAF [33] (230.748 and 226.042 $kJ\cdot mol^{-1}$, respectively) due to a slightly different choice for the enthalpy of formation of BeF_2(l) (the value retained for the model is based on the selection by Konings et al. [32]) (Table 9).

Only a few experimental studies have been reported of the vapour pressures over LiF-BeF_2 melt [43,44,65]. Berkowitz and Chupka [65] were the first to investigate a (LiF:BeF_2) = (0.5:0.5) mixture, and to identify the formation of $LiBeF_3$(g) gaseous species. Büchler and Stauffer, using a twin-crucible Knudsen effusion cell, studied LiF-BeF_2 melt in equilibrium with solid LiF (corresponding to a composition range between 66% and 79% BeF_2) and a (LiF:BeF_2) = (0.33:0.67) mixture [43]. The authors confirmed the formation of $LiBeF_3$(g) and also reported Li_2BeF_4(g) in minor amounts. The measured vapour composition above the (LiF:BeF_2) = (0.74:0.26) mixture at $T = 875$ K is compared in Fig. 20 with the computed data for this composition versus temperature. The total pressure and BeF_2(g) partial pressure are in very good agreement. The calculated partial pressures for $LiBeF_3$(g), LiF(g) and Li_3F_3(g) are two to three times higher than measured by Ref. [43]. The agreement is again very good for Li_2F_2(g). One should point out that the measurement of Ref. [43] at $T = 875$ K was done in the two-phases region {LiF + liquid}, and not above a pure melt.

More recently, Fukuda et al. measured the vapour pressure over pure BeF_2 as well as LiF-BeF_2 and NaF-BeF_2 mixtures using a combination of thermogravimetric analysis and Knudsen cell mass spectrometry [44]. The authors reported a vapour content constituted of mainly BeF_2 plus smaller quantities of $LiBeF_3$(g) and $NaBeF_3$(g) for melts in the composition range between 30% and 90% BeF_2. By contrast with Büchler and Stauffer, Fukuda et al. do not mention any $Li_2BeF^+_3$ ions detected, which could be attributed to the fragmentation pattern of the Li_2BeF_4(g) species in the Knudsen experiment. They mention only $LiBeF^+_2$, Li^+, BeF^+_2 and BeF^+ corresponding to

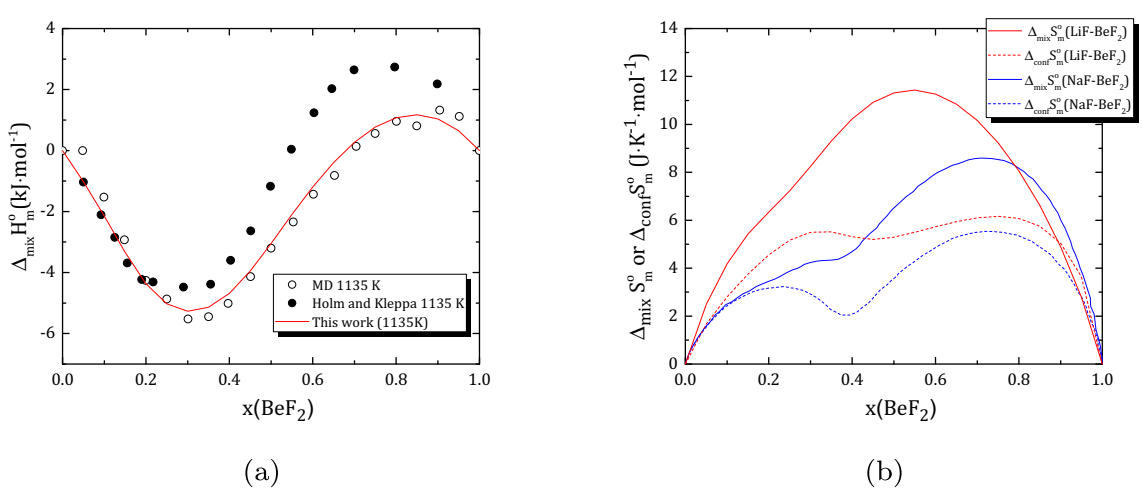

Fig. 17. (a) Calculated enthalpy of mixing for the (Li,Be)F_x liquid solution at $T = 1135$ K, and comparison with the experimental data of Holm and Kloppa [10] and results of the MD simulations. (b) Calculated entropy of mixing and configurational entropy for the (Li,Be)F_x liquid solution at $T = 1000$ K, and comparison with the computed data for the (Na,Be)F_x liquid solution at the same temperature in Ref. [34]. The configurational entropy was calculated from the formula $\Delta_{conf}S^o_m = -R\sum_i x_i \ln x_i$ where $x_i = \{x_{LiF}, x_{Be_{IV}F_2}, x_{Be_2F_4}, x_{Be_3F_6}\}$ represent the site fractions of the sublattice constituents.

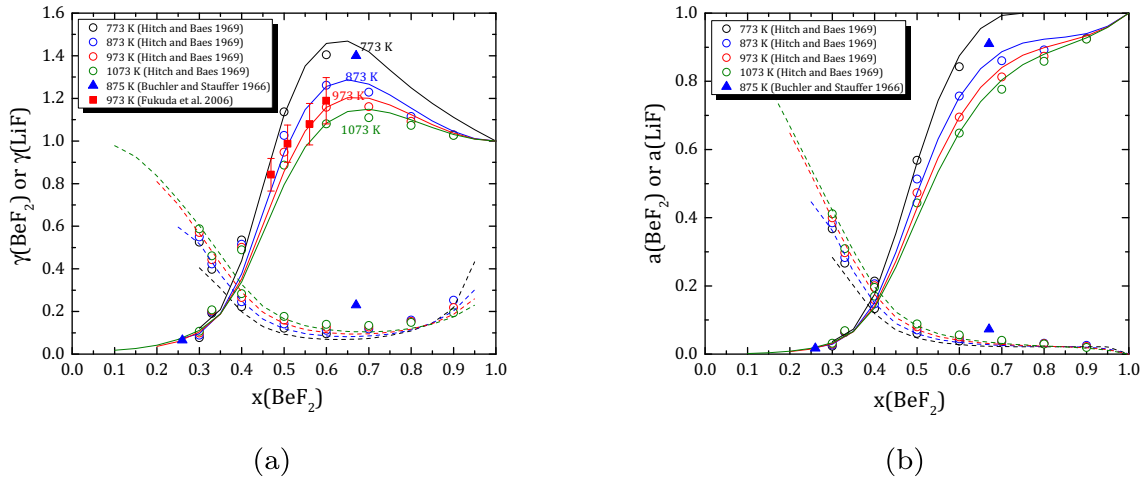

Fig. 18. Calculated activity coefficients and activities of LiF and BeF_2 in the melt at $T = 773$, 873, 973 and 1073 K and comparison with the data of Ref. [11] measured by the emf method, and the data of Refs. [43] and [44] obtained from vapour pressure measurements.

the ionization and fragmentation patterns of $LiBeF_3$(g) and BeF_2(g). In any case, its contribution is very small (0.5% of the total vapour pressure for a (LiF:BeF_2) = (0.74:0.26) melt at 875 K according to Ref. [43]). Using our model, we have computed the partial pressures and total vapour pressure of the gaseous species (not considering Li_2BeF_4) above the melt at $T = 1200$ K (see Fig. 21a). One can see that BeF_2 is largely the dominant species above $x(BeF_2) \sim 0.15$. The $LiBeF_3$ fraction reaches a maximum of about 20% at $x(BeF_2) \sim 0.2$.

The contribution of Li_2BeF_4(g) was ignored in the present model since its contribution was reported to be very minor [43], and no thermodynamic data were reported to this date for this gaseous species. For completeness, we have nevertheless estimated its standard entropy at 298.15 K and high temperature heat capacity via statistical mechanical calculations, based on the molecular parameters and spectroscopic data derived by Ramondo et al. [66] using ab initio Hartree-Fock self-consistent field calculations. Further details are given in Appendix E. The enthalpy of formation was then adjusted to fit the vapour pressure data of Büchler and Stauffer on the (LiF:BeF_2) = (0.74:0.26) composition at $T = 875$ K. The corresponding partial pressures and total vapour pressure have been recalculated at $T = 1200$ K, and are shown in the Appendix E. The effect on the total vapour pressure is negligible.

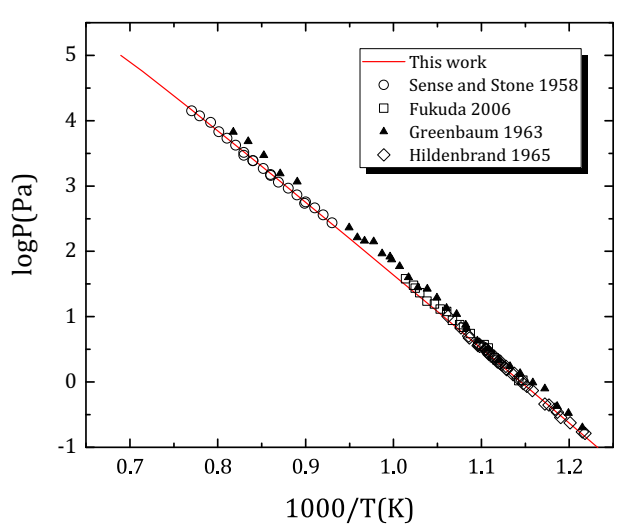

Fig. 19. Calculated vapour pressure over pure BeF_2 and comparison with the experimental data of Sense and Stone [62] (○), Greenbaum et al. [63] (▲), Hildenbrand et al. [64] (◇), and Fukuda et al. [44] (□).

Büchler and Stauffer [43] and Fukuda et al. [44] derived the thermodynamic activities of LiF and BeF_2 in the melt from their experimental measurements at $T = 875$ K and $T = 973$ K, respectively. These are compared in Fig. 18a and b with the computed data at those temperatures. The agreement with the model and the determination by Hitch and Haes using the emf method is very good.

Finally, the distribution of beryllium species $[BeF_{IV}^{2+}]$, $[Be_2F_7^{3-}]$ and $[Be_3F_{10}^{4-}]$ are calculated at $T = 900$, 1000, 1100, 1135 and 1200 K from the molar fractions of the various quadruplets according to the following relations:

$$[BeF_4^{2-}] = \frac{X_{LiBe_{IV}} + X_{Be_{IV}Be_{IV}} + X_{Be_{IV}Be_2}/2 + X_{Be_{IV}Be_3}/2}{\sum_k \sum_{l \gg k} X_{kl/F_2} - X_{LiLi}} \quad (29)$$

$$[Be_2F_7^{3-}] = \frac{X_{LiBe_2} + X_{Be_2Be_2} + X_{Be_{IV}Be_2}/2 + X_{Be_2Be_3}/2}{\sum_k \sum_{l \gg k} X_{kl/F_2} - X_{LiLi}} \quad (30)$$

$$[Be_3F_{10}^{4-}] = \frac{X_{LiBe_3} + X_{Be_3Be_3} + X_{Be_{IV}Be_3}/2 + X_{Be_2Be_3}/2}{\sum_k \sum_{l \gg k} X_{kl/F_2} - X_{LiLi}} \quad (31)$$

where k and l represent the Li^+, Be_{IV}^{2+}, Be_2^{4+}, and Be_3^{6+} cations, and X_{kl} represents the mole fraction of the (k-F-l) quadruplet.

The results are compared in Figs. 22, and D.5 with the distribution reported from the MD simulations at the same temperatures. Note that the extracted $Be_3F_{10}^{4-}$ species is assumed to represent in this model the largest "polymer", i.e. all $Be_3F_{10}^{4-}$ units plus all species with a Be nuclearity greater than 3. A model based on more polymeric units would introduce a too large number of fitting parameters. The calculated speciation reproduces well the MD results, confirming that our model is finally a good representation of both the local structure of the melt and its thermodynamic equilibrium properties.

The only difference one can point out is that the chemical speciation is quasi-independent of temperature in the MD simulations, whereas a more pronounced variation is computed in the CALPHAD model due to the introduction of temperature-dependent excess Gibbs energy parameters (Fig. 23). Such terms are needed to reproduce simultaneously the phase diagram and enthalpy of mixing data. The deviation from the MD is only seen at lower temperature, and remains acceptable. The overall agreement with available

Table 9
Vapour pressure data for pure BeF_2 calculated in this model and comparison with the literature.

$\Delta_{vap}H^o_m(BeF_2,T)$ (kJ•mol^{-1})	$\Delta_{sub}H^o_m(BeF_2,T)$ (kJ•mol^{-1})	Method	T (K)	Reference
225.4	230.8	Calc.	298.15	This work
226.042	230.748	Critical review	298.15	[33]
209.6		T	1075–1298	[62]
223.0 ± 8.4		TGA	871–986	[44]
217.1 ± 3.8		KCMS		[44]
	231.4[a] ± 4.2	TE/TC[b]	298.15	[64]
222.7 ± 0.8		KGE/T	823–1053/1123–1223	[63]

T = Transpiration; TGA = Thermogravimetric Analysis; KCMS = Knudsen Cell Mass Mass Spectrometry;
TE = Torsion-effusion; TC = Torsion-Knudsen; KGE = Knudsen gravimetric effusion.
[a] Third law value at 298.15 K.
[b] Measurements in the range 820–940 K (TE)/1175.6–1178.2 K (TC).

experimental data (i) local structure, (ii) phase diagram, (iii) mixing enthalpies, (iv) activity coefficients, and (v) vapour pressures is very satisfactory.

4.3. Assessment of the performance of the (Li,Be)F_x melt as coolant

The present work finally provides a comprehensive overview and self-consistent set of thermo-physical and thermodynamic properties for the (Li,Be)F_x melt, derived from experiments, molecular dynamics simulations and our coupled structural-thermodynamic model. This set of data is used herein to derive figures of merits (FOM) for this salt mixture to assess its performance as coolant in nuclear reactors as proposed by Bonilla [67]. Generalized heat-transfer metrics are useful to compare the suitability of coolants depending on the nature of the flow, by accounting for their performance in terms of multiple physico-chemical properties simultaneously (e.g. viscosity, heat capaciy, thermal conductivity, etc.). The FOMs suggested by Bonilla for fluoride salts are:

$$FOMi = \left(\frac{\eta^s}{\beta^t \rho^u C_p^v \lambda^w}\right)^r \tag{32}$$

where $i = \{1, 2, 3\}$, η, β, C_p, and λ are the viscosity, thermal expansion, density, massic heat capacity at constant pressure, and thermal conductivity, respectively. The set of exponents r, s, t, u, v and w depends on the nature of the flow:

- FOM1: Forced convection, turbulent regime ($r = 1, s = 0.2, t = 0, u = 2, v = 2.8$ and $w = 0$).
- FOM2: Natural convection, turbulent regime ($r = 0.36, s = 0.2, t = 1, u = 2, v = 1.8$ and $w = 0$).
- FOM3: Natural convection, laminar regime ($r = 0.5, s = 1, t = 1, u = 2, v = 1$ and $w = 0$).

The most suitable coolants are those with the smallest FOMs, which corresponds to those with low viscosity and high density, thermal expansion, heat capacity and thermal conductivity. The FOMs have been evaluated for the (Li,Be)F_x melt at $T = 900$, 1000, 1100 and 1200 K, and are shown in Fig. 24 and listed in Table 10 and Table F.1. η, β, and λ were taken from the output of the MD simulations, and C_p from the structural-thermodynamic model. The FOMs decrease with increasing temperature, which can be related to the decrease in viscosity, and increase in the thermal expansion. They also decrease with increasing LiF content, which mostly relates to a decrease in viscosity and increase in the thermal expansion.

It is also interesting to compare those FOMs with the ones reported for a fully ionic liquid such as FLiNaK (LiF-NaF-KF) [4] and a liquid forming molecular complexes such as NaF-ZrF_4 [4] and LiF-ThF_4 [60]. The figures of merits FOM1 at $T = 1000$ K and $x(BeF_2) = 0.397$ and 0.439 are about 20 times higher than reported for LiF-ThF_4 and NaF-ZrF_4 mixtures of similar composition, and 40 times higher than in FLiNaK. This result illustrates that more viscous fluids (LiF-BeF $_2$ > LiF-ThF_4, NaF-ZrF $_4$ > FLiNaK) hinder the turbulent regime and therefore its heat transfer. By contrast FOM2 and FOM3 are lower in the (Li,Be)F_x melt than they are in the other mixtures. This shows that such polymeric type of liquid becomes more advantageous in case of natural convection, irrespective of the regime (turbulent or laminar). Here the combination of thermal expansion, density, and heat capacity properties cancel out the effect of the high viscosity.

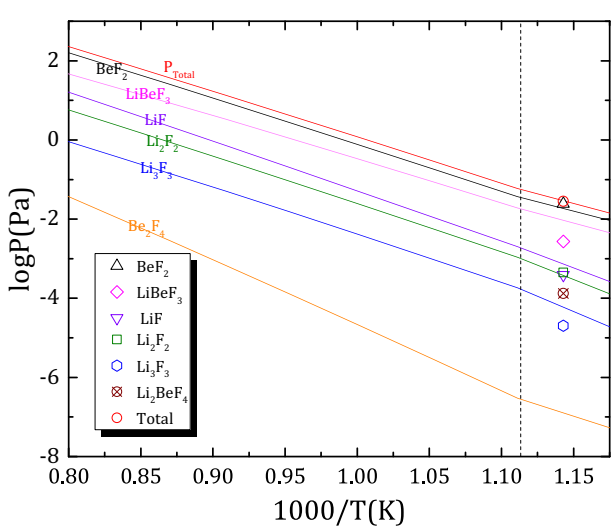

Fig. 20. Calculated vapour pressure over pure (LiF:BeF_2)=(0.74:0.26) versus temperature, and comparison with the experimental data of Büchler and Stauffer measured at $T = 875$ K using a twin-crucible Knudsen effusion cell [43].

5. Conclusions

The thermo-physical properties of the (Li,Be)F_x melt, i.e. density, thermal expansion, viscosity, thermal conductivity, have been computed from polarizable ionic interaction potentials over a much wider range of compositions and temperatures than reported previously in the literature. The calculated data have been examined with respect to available experimental information, and the predicted thermodynamic properties, i.e. enthalpies of mixing and heat capacities, have been scrutinized for the first time. The agreement is generally very good, which gives good confidence on the predictive capabilities of the PIM potentials. General trends have been discussed in relation

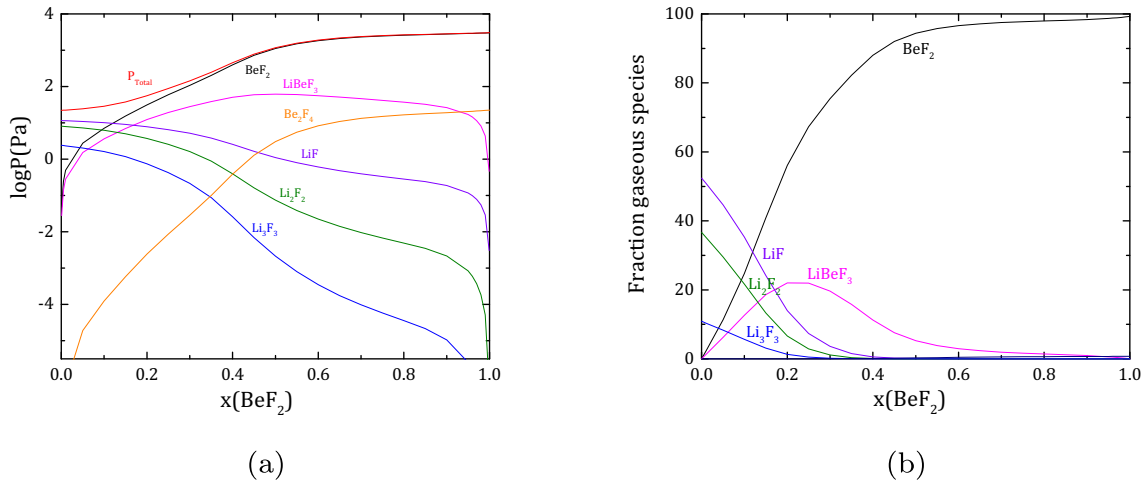

(a) (b)

Fig. 21. Calculated vapour pressure and vapour composition over (LiF:BeF_2) melt at T= 1200 K.

with the local structure of the melt. The formation of short-range order, and especially of polymeric units at high BeF_2 concentrations, can be directly related to the S-shape of the excess molar volume and enthalpies of mixing, to the energetic asymmetry of the activity and activity coefficients data, or to the drastic increase in viscosity with increasing BeF_2 content. The transition between a molecular type of

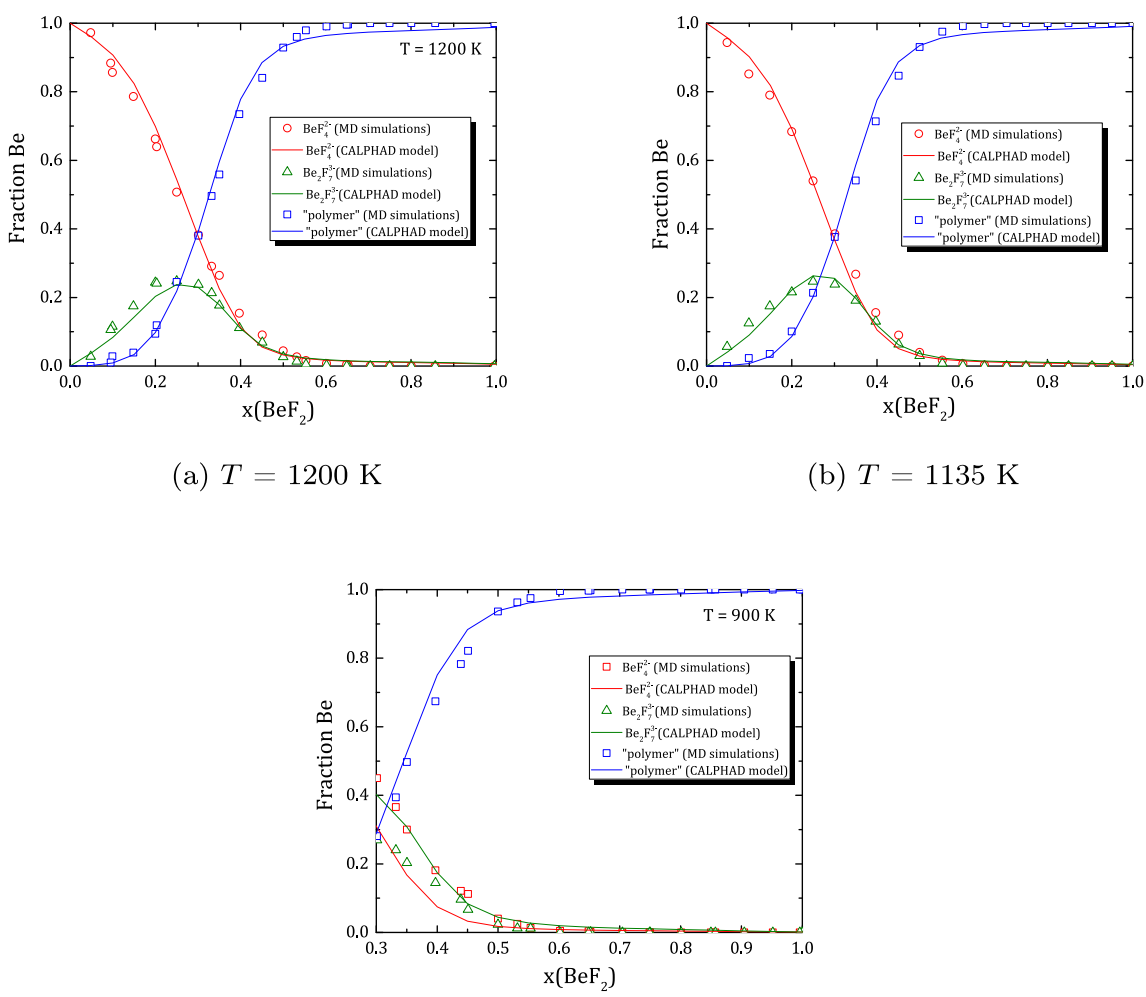

(a) T = 1200 K (b) T = 1135 K

(c) T = 900 K

Fig. 22. Distribution of BeF_4^{2-}, $Be_2F_7^{3-}$ and $Be_3F_{10}^{4-}$ species calculated in the liquid at T = 900, 1135 and 1200 K, and comparison with the output of the MD simulations; "polymer" means a cluster with a Be nuclearity equal or greater than 3.

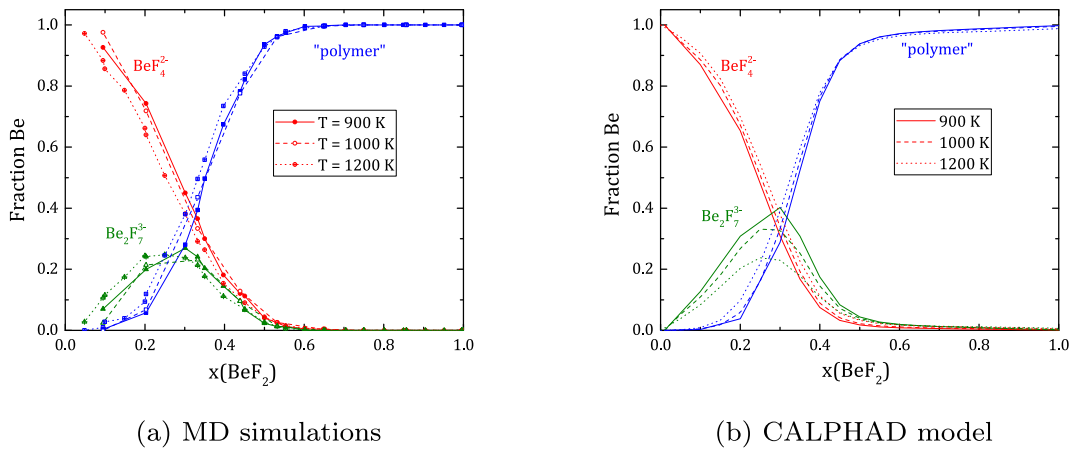

Fig. 23. Distribution of BeF_4^{2-}, $Be_2F_7^{3-}$ and $Be_3F_{10}^{4-}$ species calculated in the liquid at $T = 900$, 1000 and 1200 K from the coupled structural-thermodynamic model and from the MD simulations; "polymer" means a cluster with a Be nuclearity equal or greater than 3.

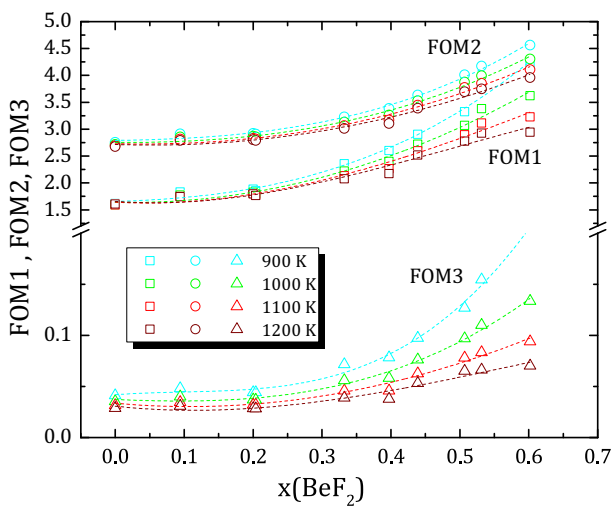

Fig. 24. Variation of the figures of merits FOM1, FOM2, and FOM3 as defined in the text for the $(Li,Be)F_x$ melt at $T = 900$, 1000, 1100 and 1200 K.

liquid and a polymeric type of liquid around $x(BeF_2) \sim 0.2$–0.3 is also seen in the density evolution which shows a maximum around $x(BeF_2) \sim 0.3$. The MD calculations are very useful to identify subtle deviations from an ideal behaviour. The example of the excess molar volume is particularly striking. A linear evolution as a function of composition could be assumed based on experimental measurements, whereas the simulations are able to reveal the asymmetric evolution. Because MD simulations are not well suited by definition to characterize thermodynamic phase equilibria, it is very appealing to combine them with a semi-empirical approach such as the CALPHAD methodology, that is able to predict the equilibrium state of a system. In this work, a comprehensive structural-thermodynamic model of the LiF-BeF_2 system is therefore reported that brings together the output of the experimental thermodynamic data and MD simulations. The model, based on the quasi-chemical formalism in the quadruplet approximation, reproduces well equilibrium thermodynamic data, excess properties, and local structure of the melt, in particular the distribution of Li^+, F^-, BeF_4^{2-}, $Be_2F_7^{3-}$, $Be_3F_{10}^{4-}$ polymeric units as a function of composition. This methodology is a step towards multi-scale modelling of the salt combining atomistic simulations and thermodynamic modelling. The next stage would be the coupling with multi-physics tools such as thermo-hydraulics codes to provide a complete picture of the molten salt fuel behaviour in a MSR under any set of conditions.

Declaration of Competing Interest

The authors declare that they have no known competing financial interests or personal relationships that could have appeared to influence the work reported in this paper.

Acknowledgments

A.L. Smith acknowledges gratefully financial support from the Netherlands Organisation for Scientific Research (NWO) (project 722.016.005). The authors would also like to thank M. Salanne (UPMC University Paris 06) for sharing with us his calculation codes for the chemical speciation. Computational resources for this work were provided by the Réseau Québecois de Calcul de Haute Performance (RQCHP).

Table 10
Figures of merits of $(Li,Be)F_x$, $(Li,Th)F_x$, $(Na,Zr)F_x$ and $(Li,Na,K)F_x$ melts.

Melt	T (K)	FOM1	FOM2	FOM3	Ref
$(LiF:BeF_2) = (0.561:0.439)$	1000	2.720	3.528	0.076	This work
$(NaF:ZrF_4) = (0.57:0.43)$	973	0.126	8.98	41.74	[4]
$(LiF:BeF_2) = (0.603:0.397)$	1000	2.399	3.262	0.058	This work
$(LiF:ThF_4) = (0.603:0.397)$	1025	0.145	8.898	46.217	[60]
$(LiF:NaF:KF) = (0.465:0.115:0.42)$	973	0.063	8.01	31.45	[4]

Appendix A. Molar volumes

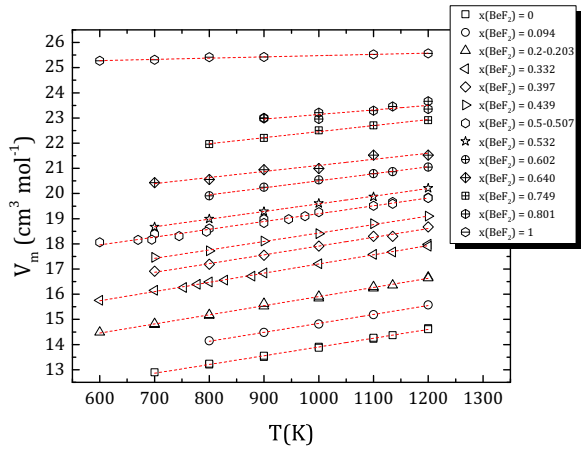

Fig. A.1. Evolution of the molar volume as a function of temperature and composition as derived from the MD simulations.

Appendix B. Chemical speciation calculated from the MD simulations

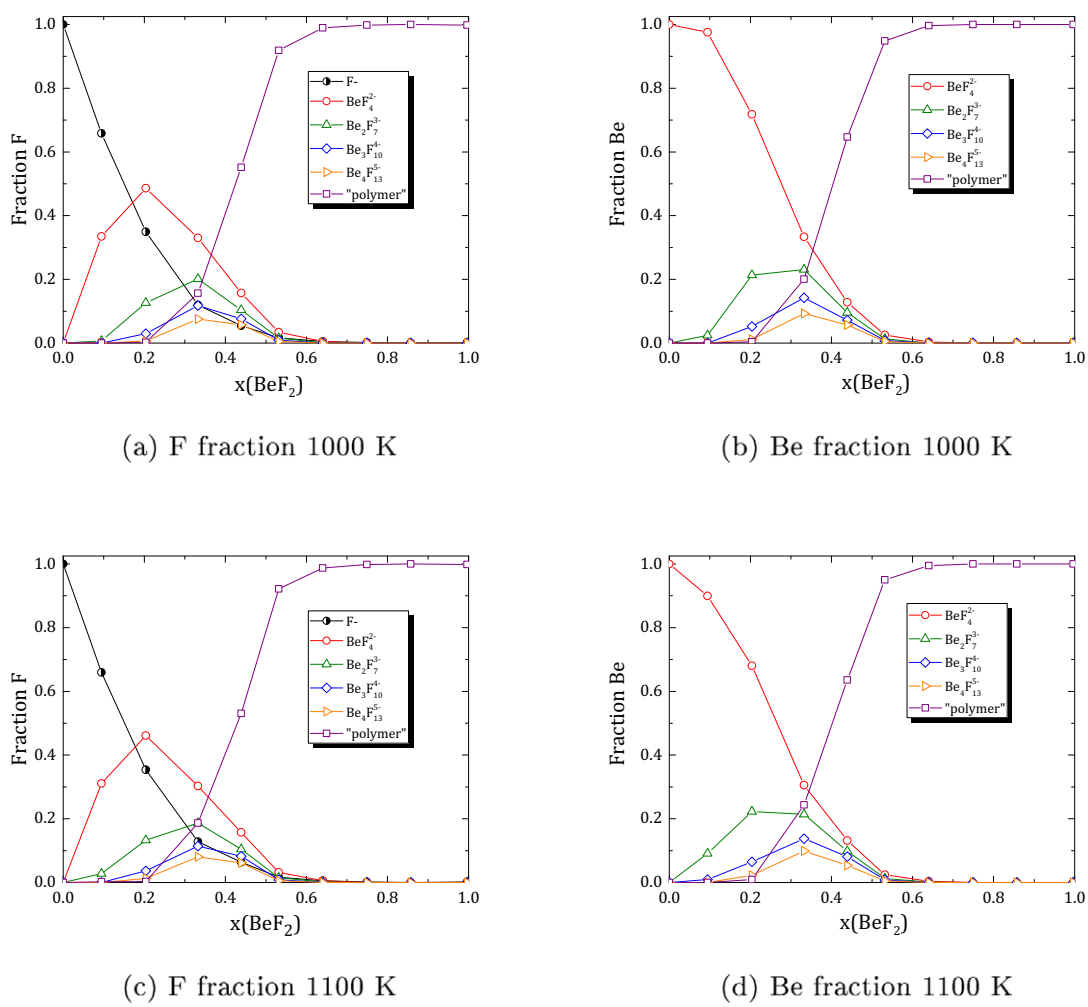

Fig. B.2. Fraction of F atoms and Be atoms involved in various species observed in the system as a function of composition at $T = 1000$ and 1100 K; "polymer" means a cluster with a Be nuclearity greater than 4, whereas F^- implies that the ion is coordinated only to Li^+.

Appendix C. Molar enthalpies

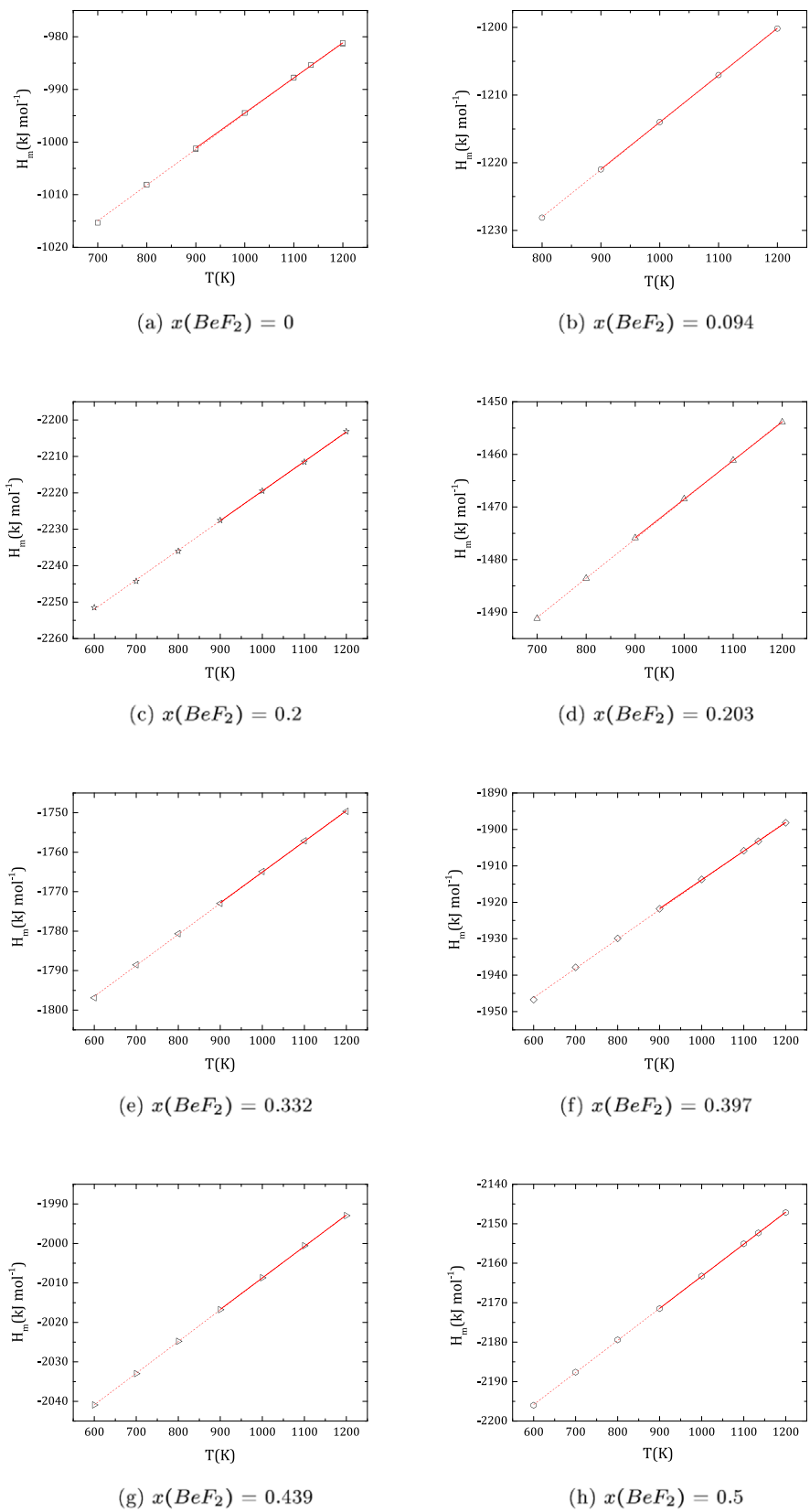

(a) $x(BeF_2) = 0$

(b) $x(BeF_2) = 0.094$

(c) $x(BeF_2) = 0.2$

(d) $x(BeF_2) = 0.203$

(e) $x(BeF_2) = 0.332$

(f) $x(BeF_2) = 0.397$

(g) $x(BeF_2) = 0.439$

(h) $x(BeF_2) = 0.5$

Fig. C.3. Molar enthalpies derived from the MD simulations and fit to the data.

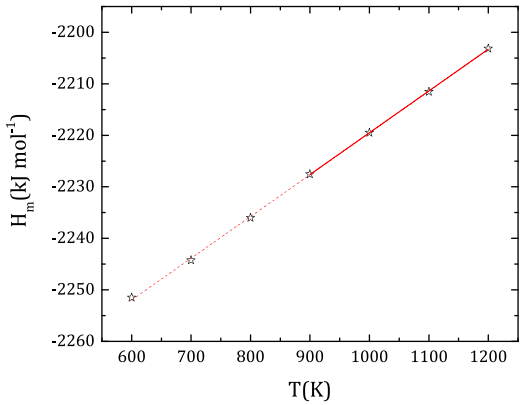

(a) $x(BeF_2) = 0.532$

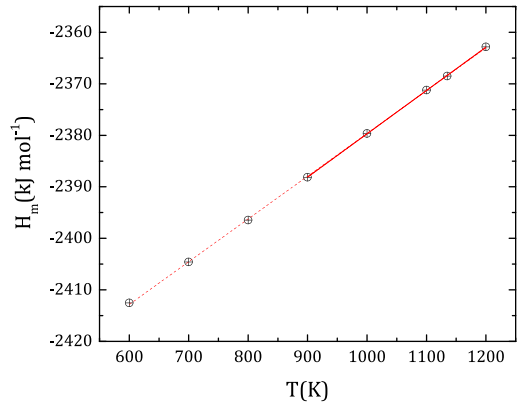

(b) $x(BeF_2) = 0.601$

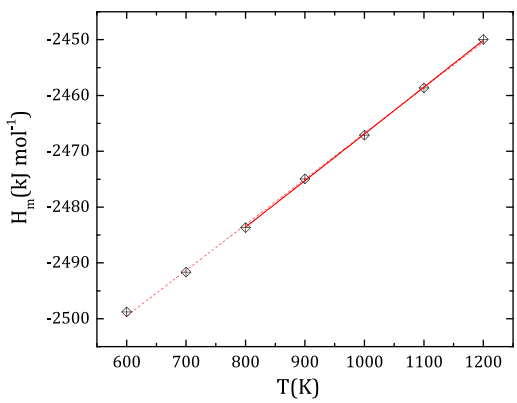

(c) $x(BeF_2) = 0.640$

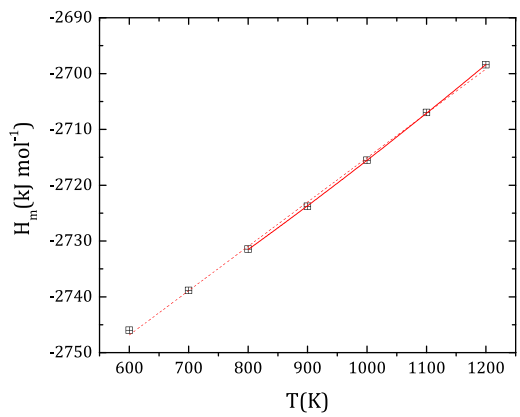

(d) $x(BeF_2) = 0.749$

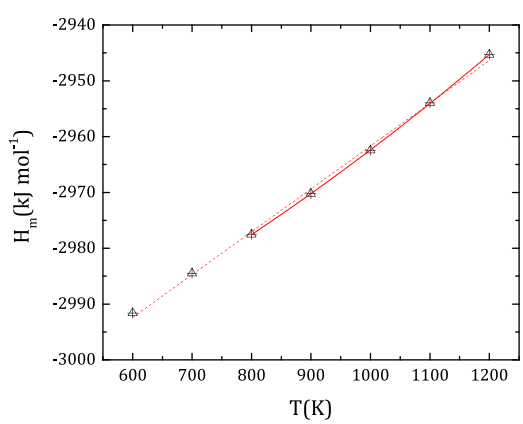

(e) $x(BeF_2) = 0.857$

Fig. C.4. Molar enthalpies derived from the MD simulations and fit to the data.

Appendix D. Chemical speciation from the coupled structural-thermodynamic model

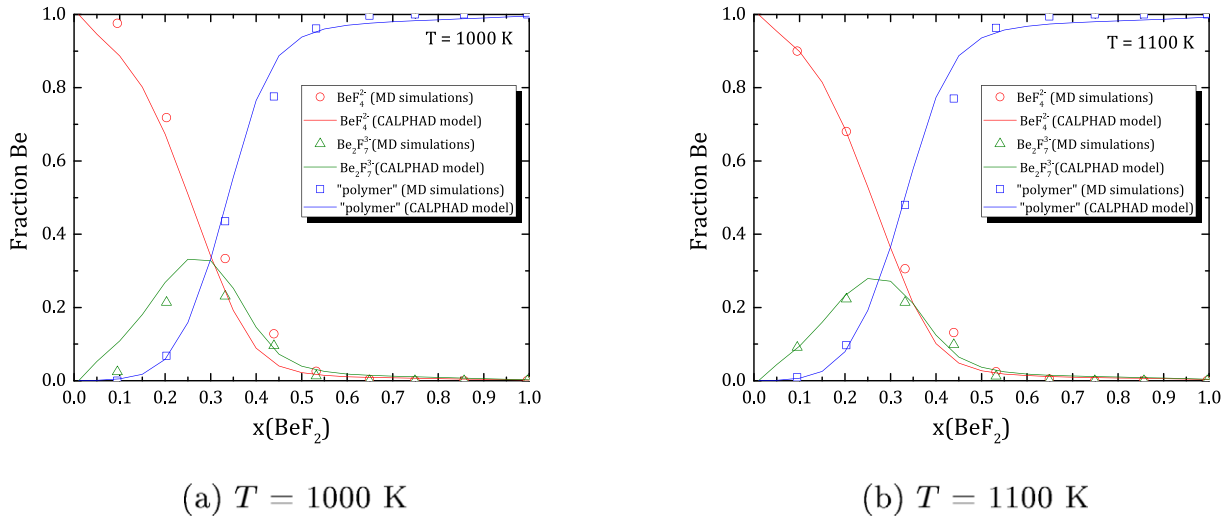

Fig. D.5. Distribution of BeF_4^{2-}, $Be_2F_7^{3-}$ and $Be_3F_{10}^{4-}$ species calculated in the liquid at $T = 1000$ and 1100 K, and comparison with the output of the MD simulations; "polymer" means a cluster with a Be nuclearity equal or greater than 3.

Appendix E. Calculation of thermodynamic functions of Li_2BeF_4(g)

The thermodynamic functions of the Li_2BeF_4 gaseous molecule have been determined here via statistical mechanical calculations. The classical rigid rotor and harmonic oscillator approximations were used for the computations, which were performed using a set of Fortran codes as described in Refs.[68,69]. The input parameters, i.e. the molecular parameters and the spectroscopic data of the molecule, were taken from the work of Ramondo et al., who found the D_{2d} configuration to be the most stable for this molecule. The derived values for the standard entropy at 298.15 K is:

$$S^{o}_{m}(Li_2BeF_4, g, 298.15\ \mathrm{K}) = 331.3\ \mathrm{J{\cdot}K^{-1}{\cdot}mol^{-1}} \tag{E.1}$$

The derived heat capacity function for the temperature range 298.15 –3000 K is:

$$C^{o}_{p,m}(Li_2BeF_4, g, T) = 179.47 - 9.47{\cdot}10^{-3}T + 166{,}240.9{\cdot}T^{-2} + \\ + 1.45377{\cdot}10^{-6}T^2 - 20{,}474.7{\cdot}T^{-1}\ \mathrm{J{\cdot}K^{-1}{\cdot}mol^{-1}} \tag{E.2}$$

The enthalpy of formation at 298.15 K was optimized in this work to fit the vapour pressure data of Büchler and Stauffer on the $(LiF{:}BeF_2) = (0.74{:}0.26)$ composition at $T = 875$ K [43] as described previously. The derived value is:

$$\Delta H^{o}_{m}(Li_2BeF_4, g, 298.15\ \mathrm{K}) = -1972.0\ \mathrm{kJ{\cdot}mol^{-1}} \tag{E.3}$$

The corresponding partial pressures and total vapour pressure are shown in Fig. E.6a. The calculated partial pressure of Li_2BeF_4(g) at $T = 875$ K is in very good agreement with the experimental data [43] and the effect on the total vapour pressure is negligible. The vapour pressures over $(LiF{:}BeF_2)$ melt at $T = 1200$ K have also been recalculated considering Li_2BeF_4 among the gaseous species and are shown in Fig. E.6b.

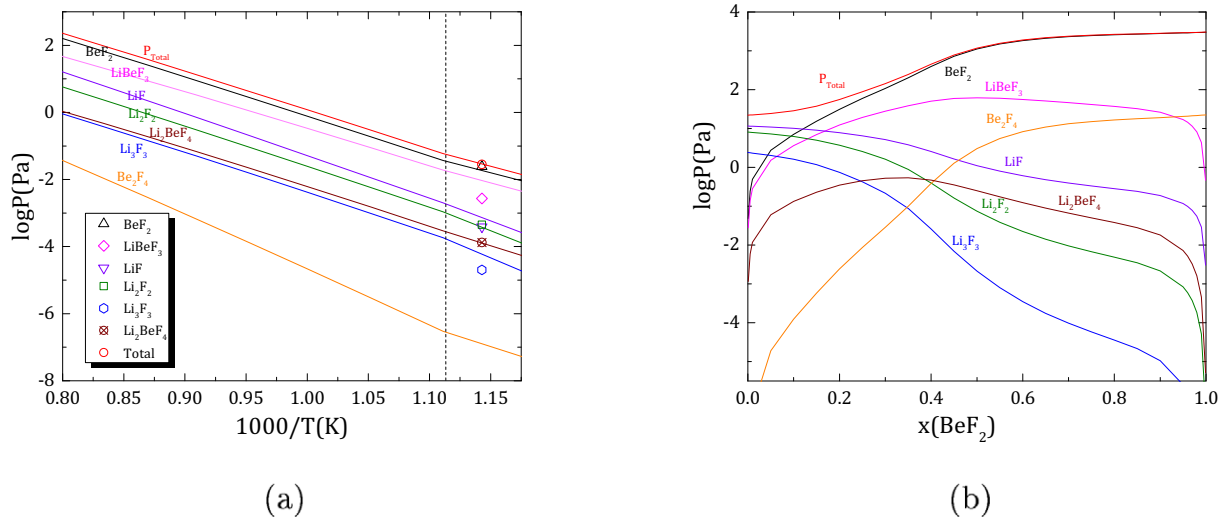

Fig. E.6. (a) Calculated vapour pressure over pure ($LiF:BeF_2$) = (0.274:0.26) versus temperature considering Li_2BeF_4(g) among the gaseous species, and comparison with the experimental data of Büchler and Stauffer measured at T = 875 K using a twin-crucible Knudsen effusion cell [43]. (b) Calculated vapour pressure over ($LiF:BeF_2$) melt at T= 1200 K considering Li_2BeF_4(g) among the gaseous species.

Appendix F. Figures of merits

Table F.1
Figures of merits in the (Li,Be)F_x melt at T = 900, 1000, 1100 and 1200 K.

$x(BeF_2)$	T (K)	FOM1	FOM2	FOM3
0	900	1.615	2.756	0.041
0.094	900	1.829	2.912	0.048
0.203	900	1.851	2.910	0.044
0.332	900	2.357	3.226	0.072
0.397	900	2.603	3.383	0.078
0.439	900	2.902	3.635	0.097
0.507	900	3.321	4.011	0.127
0.532	900	3.764	4.175	0.155
0.602	900	4.200	4.562	0.206
0	1000	1.593	2.717	0.036
0.094	1000	1.775	2.855	0.040
0.203	1000	1.796	2.855	0.037
0.332	1000	2.219	3.133	0.056
0.397	1000	2.399	3.262	0.058
0.439	1000	2.720	3.528	0.076
0.507	1000	3.070	3.876	0.097
0.532	1000	3.380	3.993	0.110
0.602	1000	3.622	4.304	0.134
0	1100	1.592	2.692	0.032
0.094	1100	1.749	2.816	0.035
0.203	1100	1.770	2.817	0.032
0.332	1100	2.131	3.064	0.046
0.397	1100	2.263	3.171	0.046
0.439	1100	2.599	3.448	0.063
0.507	1100	2.896	3.774	0.078
0.532	1100	3.113	3.855	0.083
0.602	1100	3.226	4.109	0.094
0	1200	1.607	2.678	0.029
0.094	1200	1.743	2.789	0.031
0.203	1200	1.764	2.791	0.028
0.332	1200	2.078	3.014	0.039
0.397	1200	2.173	3.103	0.038
0.439	1200	2.520	3.388	0.053
0.507	1200	2.775	3.695	0.065
0.532	1200	2.925	3.749	0.066
0.602	1200	2.944	3.956	0.070

Appendix G. Supplementary data

Supplementary data to this article can be found online at https://doi.org/10.1016/j.molliq.2019.112165.

References

[1] O. Beneš, R.J.M. Konings, Comprehensive Nuclear Materials, Chapter 3.13: Molten salt reactor fuel and coolant, 1st ed. ed., vol. 3. Elsevier Inc.. 2012.
[2] D.F. Williams, L.M. Toth, K.T. Clarno, Assessment of Candidate Molten Salt Coolants for the Advanced High-Temperature Reactor (AHTR), Technical Report, ORNL/TM-2006/12, Oak Ridge National Laboratory. 1968,
[3] T. Ihli, T.K. Basu, L.M. Giancarli, S. Konishi, S. Malang, F. Najmabadi, S. Nishio, A.R. Raffray, C.V.S. Rao, A. Sagara, Y. Wu, Fusion Eng. Des. 83 (2008) 912–919.
[4] M. Salanne, C. Simon, P. Turq, P. Madden, J. Fluor. Chem. 130 (2009) 38–44.
[5] V. Dracopoulos, B. Gilbert, G. Papatheodorou, J. Chem. Soc. Faraday Trans. 94 (1998) 2601–2604.
[6] D.M. Roy, R. Roy, E.F. Osborn, J. Am. Ceram. Soc. 33 (3) (1950) 85–90.
[7] D.M. Roy, R. Roy, E.F. Osborn, J. Am. Ceram. Soc. 37 (1954) 300–305.
[8] R.E. Thoma, H. Insley, H.A. Friedman, G.M. Hebert, J. Nucl. Mater. 27 (1968) 166–180.
[9] K.A. Romberger, J. Braunstein, R.E. Thoma, J. Phys. Chem. 76 (1972) 1154–1159.
[10] J.L. Holm, O.J. Kleppa, Inorg. Chem. 8(2) (1969) 207–212.
[11] B.F. Hitch, C.F. Baes, Inorg. Chem. 8 (1969) 201–207.
[12] C.E. Vallet, J. Braunstein, J. Am. Ceram. Soc. 60 (1977) 315–317.
[13] S. Cantor, J.W. Cooke, A.S. Dworkin, G.D. Robbins, R.E. Thoma, G.M. Watson, ORNL-TM-2316, Technical Report, ORNL-TM-2316, Oak Ridge National Laboratory. 1968,
[14] T.B. Douglas, W.H. Payne, J. Res. NBS 73A (1969) 479.
[15] S. Cantor, W. Ward, C. Moynihan, J. Chem. Phys. 50 (1969) 2874–2879.
[16] S. Cantor, Density and Viscosity of Several Molten Fluoride Mixtures, ORNL-TM-4308, Oak Ridge National Laboratory. 1973.Technical report.
[17] J.W. Cooke, H.W. Hoffman, J.J. Keyes, ORNL-TM-4396, ORNL-TM-4396, Oak Ridge National Laboratory. 1969.Technical report.
[18] Y. Kato, K. Furukawa, N. Araki, Y. Kato, High Temp. High Pres. 15 (1983) 191–198.
[19] H.L. Lukas, S.G. Fries, B. Sundman, Computational Thermodynamics. The Calphad Method., Cambridge University Press. 2007.
[20] J.P.M.V. der Meer, R.J.M. Konings, M.H.G. Jacobs, H.A.J. Oonk, J. Nucl. Mater. 344 (2005) 94–99.
[21] O. Beneš, R.J.M. Konings, J. Chem. Thermodyn. 41 (2009) 1086–1095.
[22] A. Romero-Serrano, M. Hallen-Lopez, B. Zeifert, C. Gomez-Yan, A. Hernandez-Ramirez, J. Fluor. Chem. 130 (2009) 336–340.
[23] P. Lin, A. Pelton, Metall. Mater. Trans. B 10B (1979) 667–676.
[24] A. Romero-Serrano, A. Pelton, Metall. Mater. Trans. B 26 (1995) 305–315.
[25] R. Heaton, R. Brookes, P. Madden, M. Salanne, C. Simon, P. Turq, J. Phys. Chem. B 110 (2006) 11454–11460.
[26] M. Salanne, C. Simon, P. Turq, R. Heaton, P. Madden, J. Phys. Chem. B 110 (2006) 11461–11467.
[27] M. Salanne, C. Simon, P. Turq, P. Madden, J. Phys. Chem. B 111 (2007) 4678–4684.
[28] P. Madden, M. Salanne, Thorium molten salts: theory and practice, Thorium Energy for the World: Proceedings of the ThEC13 Conference, CERN, Globe of Science and Innovation, Geneva, Switzerland, October 27–31, 2013, Springer. 2016, pp. 111–116.
[29] P. Madden, M. Wilson, Chem. Soc. Rev. 25 (1996) 339–350.
[30] F. Hutchinson, M. Wilson, P. Madden, Mol. Phys. 99 (2001) 811–824.
[31] C. Bale, E. Bélisle, P. Chartrand, S. Decterov, G. Eriksson, A. Gheribi, K. Hack, I.-H. Jung, Y.-B. Kang, J. Melançon, A. Pelton, S. Petersen, C. Robelin, J. Sangster, P. Spencer, M.-A.V. Ende, Calphad 54 (2016) 35–53.
[32] R.J.M. Konings, J.P.M. van der Meer, E. Walle, Chemical aspects of molten salt reactor fuel, Tech. report ITU-TN 2005/25, Technical Report, Institute for Transuranium Elements. 2005,
[33] M.W. Chase, NIST-JANAF Thermochemical Tables (Journal of Physical and Chemical Reference Data Monograph No. 9), 1998.
[34] C. Robelin, P. Chartrand, J. Chem. Thermodyn. 57 (2013) 387–403.
[35] A.D. Pelton, S.A. Degterov, G. Eriksson, C. Robelin, Y. Dessureault, Metall. Mater. Trans. B 31 (4) (2000) 651–659.
[36] A.S. Quist, J.B. Gates, G.E. Boyd, J. Phys. Chem. 76(1) (1972) 78–83.
[37] L.M. Toth, J.B. Gates, G.E. Boyd, J. Phys. Chem. 77(2) (1973) 216–221.
[38] S. Liu, T. Su, J. Cheng, X. An, P. Zhang, H. Liu, S. Yao, L. Xie, H. Hou, J. Mol. Liq. 242 (2017) 1052–1057.
[39] J. Dai, H. Han, Q. Li, P. Huai, J. Mol. Liq. 213 (2016) 17–22.
[40] A.D. Pelton, P. Chartrand, G. Eriksson, Metall. Mater. Trans. A 32 (2001) 1409–1416.
[41] A.D. Pelton, P. Chartrand, Metall. Mater. Trans. A 32 (2001) 1417–1430.
[42] A.D. Pelton, P. Chartrand, Metall. Mater. Trans. A 32 (2001) 1355–1360.
[43] A. Büchler, J.L. Stauffer, Vaporization in the lithium fluoride-beryllium fluoride system, Symposium on Thermodynamics of Nuclear Materials, IAEA Proc. Series No. 109, Internatioal Atomic Energy Agency, 1966, pp. 271–290.
[44] G.T. Fukuda, P.F. Peterson, D.R. Olander, Vapor pressure measurements on mixtures of LiF, NaF, and BeF2, 21st IEEE/NPS Symposium on Fusion Engineering SOFE 05, Knoxville, TN, USA, 26–29 Sept. 2005, 2006, pp. 324–327.
[45] B.C. Blanke, E.N. Bousquet, M.L. Curtis, E.L. Murphy, USAEC MLM-1086, Technical Report, 1956,
[46] O. Pauvert, M. Salanne, D. Zanghi, C. Simon, S. Reguer, D. Thiaudiére, Y. Okamoto, H. Matsuura, C. Bessada, J. Phys. Chem. B 115 (2011) 9160–9167.
[47] S.I. Cohen, T.N. Jones, ORNL-2278, Technical Report, 1957,
[48] Y. Abe, O. Kosugiyama, A. Nagashima, J. Nucl. Mater. 99 (1981) 173–183.
[49] V.N. Desyatnik, A.I. Nechaev, Y.F. Chervinskii, Zh. Prikl. Khim. 54 (1981) 2310–2313.
[50] Y. Nagasaka, A. Nagashima, Int. J. Thermophys. 14 (4) (1993) 923–936.
[51] V.D. Golyshev, M.A. Gonik, V.A. Petrov, Y.M. Putilin, Teplofiz. Vysok. Temp. 21 (1983) 899–903.
[52] V.D. Golyshev, M.A. Gonik, High-temperature thermophysical properties of non-scattering semitransparent materials III: thermal conductivity of melts., High Temp. High Press. 24 (1992) 677–688.
[53] A.N. Alabovskii, I.E. Veneraki, V.A. Sokolov, O.E. Khlebnikov, Prom. Teplotekh. 3 (5) (1981) 97–101.
[54] M.V. Smirnov, V.A. Khokhlov, E.S. Filatov, Electrochim. Acta 32 (7) (1987) 1019–1026.
[55] K. Sreenivasan, The School of the Thesis,(Ph.D. thesis). University of Pennsylvania. 1967.
[56] N. Ohtori, T. Oono, K. Takase, J. Chem. Phys. 130 (2009)
[57] K. Takase, I. Akiyama, N. Ohtori, Proc. Electrochem. Soc. 99-41 (Molten Salts XII) (2000) 376–382.
[58] A.E. Gheribi, J.A. Torres, P. Chartrand, Sol. Energy Mater. Sol. Cells 126 (2014) 11–25.
[59] A.E. Gheribi, P. Chartrand, J. Chem. Phys. 144 (2016) 084–506.
[60] A.E. Gheribi, D. Corradini, L. Dewan, P. Chartrand, C. Simon, P.A. Madden, M. Salanne, Mol. Phys. 112 (2014) 1305–1312.
[61] R. DiGuilio, A. Teja, Int. J. Thermophys. 13 (1992) 855–871.
[62] K.A. Sense, R.W. Stone, J. Phys. Chem. 62 (1958) 453–457.
[63] M. Greenbaum, J.N. Foster, M.L. Arin, M. Farber, J. Phys. Chem. 67 (1963) 36–40.
[64] D.L. Hildenbrand, L.P. Theard, J. Chem. Phys. 42 (1965) 3230–3236.
[65] J. Berkowitz, W.A. Chupka, Ann. N. Y. Acad. Sci. 79 (1960) 1073.
[66] F. Ramondo, L. Bencivenni, M. Spoliti, J. Mol. Struct. 277 (1992) 171–184.
[67] C. Bonilla, Nuclear Engineering Handbook, chapter 6.5, 1958, 9–90.
[68] E.H.P. Cordfunke, R.J.M. Konings, J. Phase Equilib. 14 (4) (1993) 457–464.
[69] E. Capelli, R.J.M. Konings, J. Fluor. Chem. 208 (2018) 55–64.

Update

Journal of Molecular Liquids
Volume 314, Issue , 15 September 2020, Page

DOI: https://doi.org/10.1016/j.molliq.2020.113421

Journal of Molecular Liquids 314 (2020) 113421

Contents lists available at ScienceDirect

Journal of Molecular Liquids

journal homepage: www.elsevier.com/locate/molliq

Erratum

Erratum to: "A new approach for coupled modelling of the structural and thermo-physical properties of molten salts. Case of a polymeric liquid LiF-BeF_2"

A.L. Smith [a,*], E. Capelli [a], R.J.M. Konings [b], A.E. Gheribi [c]

[a] Delft University of Technology, Faculty of Applied Sciences, Radiation Science & Technology Department, Mekelweg 15, 2629 JB Delft, the Netherlands
[b] European Commission, Joint Research Centre (JRC), Directorate for Nuclear Safety and Security, Postfach 2340, D-76125 Karlsruhe, Germany
[c] Centre for Research in Computational Thermochemistry, Department of Chemical Engineering, Ecole Polytechnique, C.P. 6079, Succursale "Downtown", Montreal, Quebec H3C 3A7, Canada

The optimized Gibbs energies for the second-nearest neighbours exchange reactions of the liquid solution were not reported correctly in Eqs. (17)–(19) in our recent work [1]. The corresponding equations should read:

$$\Delta g_{LiBe_{IV}/F_2}/\left(J\cdot mol^{-1}\right) = -25000-6.2(T/K)+2000\chi_{LiBe_{IV}/F_2} \quad (1)$$

$$\Delta g_{LiBe_2/F_2}/\left(J\cdot mol^{-1}\right) = -35800-6.2(T/K) \quad (2)$$

$$\begin{aligned}\Delta g_{LiBe_3/F_2}/\left(J\cdot mol^{-1}\right) = &-12300-22.5(T/K)\\ &+(20000-21.3(T/K))\chi_{Be_3Li/F_2}\\ &+12900\chi^2_{Be_3Li/F_2}\end{aligned} \quad (3)$$

Declaration of competing interest

The authors declare that they have no known competing financial interests or personal relationships that could have appeared to influence the work reported in this paper.

Acknowledgements

A.L. Smith acknowledges gratefully financial support from the Netherlands Organisation for Scientific Research (NWO) (project 722.016.005).

References

[1] A.L. Smith, E. Capelli, R.J.M. Konings, A.E. Gheribi, Journal of Molecular Liquids 299 (2020) 112165.

DOI of original article: https://doi.org/10.1016/j.molliq.2019.112165.

* Corresponding author.
E-mail address: a.l.smith@tudelft.nl (A.L. Smith).

https://doi.org/10.1016/j.molliq.2020.113421
0167-7322/© 2020 The Authors. Published by Elsevier B.V. This is an open access article under the CC BY license (http://creativecommons.org/licenses/by/4.0/).